



Hydrodeoxygenation of phenol over zirconia supported Pd bimetallic catalysts. The effect of second metal on catalyst performance



Karen A. Resende^a, Camila A. Teles^{b,c}, Gary Jacobs^{d,e}, Burtron H. Davis^d, Donald C. Cronauer^f, A. Jeremy Kropf^f, Christopher L. Marshall^f, Carla E. Hori^a, Fabio B. Noronha^{b,c,*}

^a Federal University of Uberlândia, School of Chemical Engineering, Av. João Naves de Ávila, 2121, Bloco 1K, Uberlândia, 38400-098, Brazil

^b National Institute of Technology, Catalysis Division, Av. Venezuela 82, Rio de Janeiro, 20081-312, Brazil

^c Military Institute of Engineering, Chemical Engineering Department, Praça Gal. Tibúrcio 80, Rio de Janeiro, 22290-270, Brazil

^d University of Kentucky, Center for Applied Energy Research, 2540 Research Park Dr., Lexington, KY 40511, USA

^e University of Texas at San Antonio, Chemical Engineering Program – Department of Biomedical Engineering, Department of Mechanical Engineering, One UTSA Circle, San Antonio, TX 78249 USA

^f Argonne National Laboratory, Argonne, IL 60439, USA

ARTICLE INFO

Keywords:

Phenol
Bio-oil
Hydrodeoxygenation
Stability
Bimetallic catalysts
Oxophilic sites

ABSTRACT

This work investigated the effect of the addition of a second metal (Cu, Ag, Zn, Sn) on the performance of Pd/ZrO₂ catalyst for HDO of phenol at 573 K in the gas phase. The incorporation of dopants resulted in the formation of Pd-X (Cu, Ag, Zn) alloys, which reduced the reaction rate for HDO and increased the selectivity to hydro-generation products (cyclohexanone and cyclohexanol). For PdSn/ZrO₂, alloying was also observed but tin oxide was still present on the surface after reduction at 773 K. For Pd/ZrO₂ and PdSn/ZrO₂, the oxophilic sites represented by Zr and Sn cations promotes the hydrogenation of the carbonyl group of the keto-tautomer intermediate formed, producing benzene as the main product. All catalysts significantly deactivated during the reaction but the deactivation degree depended on the type of the metal. Pd/ZrO₂ and PdZn/ZrO₂ and PdAg/ZrO₂ exhibited approximately the same deactivation degree. However, the loss of activity was less pronounced for PdSn/ZrO₂ catalyst. Pd dispersion significantly decreased during the reaction, indicating that the sintering of Pd particles is one of the causes for catalyst deactivation.

1. Introduction

The lignocellulosic biomass may be converted into biofuels by different technologies [1,2]. The conversion of biomass into bio-oil through fast pyrolysis followed by its upgrading by hydrodeoxygenation (HDO) is considered a potential route for the production of renewable fuels [3]. The bio-oil produced is composed of a very complex mixture of oxygenated compounds with high water content. The presence of highly reactive oxygenated compounds renders the bio-oil unstable during storage. Therefore, bio-oil must be upgraded to be feasible as a transportation fuel [4,5].

Due to the complex composition of bio-oil, a significant number of studies reported the use of model molecules to elucidate the HDO reaction mechanism [5–7]. Those compounds are chosen to represent different fractions of biomass such as sugars and sugar alcohols (celulose and hemi-cellulose), as well as phenolic compounds such as cresols, guaiacol, and phenol (*i.e.*, the lignin fraction of biomass) [5].

Different catalysts have been reported for HDO reactions of several

molecules [4–7]. Despite of all the research efforts, the development of an appropriate catalyst for HDO reaction is still an issue. The optimal catalyst for bio-oil upgrading should exhibit high activity for deoxygenation and stability under reaction conditions [6].

Currently the greatest challenge in developing new catalysts for the HDO reaction is improving the stability. Catalyst deactivation is generally attributed to the deposition of carbonaceous species on the catalyst surface or sintering of the metallic particles [3]. Therefore, understanding of the catalyst deactivation mechanisms for HDO of bio-oils is needed to design efficient catalysts. However, the number of studies dedicated to catalyst deactivation during HDO reaction is scarce.

The HDO reaction requires a metallic site for hydrogenation/dehydrogenation as well as a support that adsorbs the oxy compound and promotes alkylation and polymerization reactions. Therefore, control of the metal particle size and the selection of the support with appropriate properties may inhibit catalyst deactivation.

The addition of a second metal may induce changes in both catalytic and adsorptive properties. The dilution or the coverage of a fraction of

* Corresponding author at: National Institute of Technology, Catalysis Division, Av. Venezuela 82, Rio de Janeiro, 20081-312, Brazil.
E-mail address: fabio.bellot@int.gov.br (F.B. Noronha).

the surface of the host metal (*i.e.*, geometric effects) induces a decrease in the size of the ensemble, and this inhibits the formation of carbon. Furthermore, it may also suppress metal particle sintering. Therefore, the addition of a second metal induces changes in selectivity, affecting more severely reactions involving C–C bond scission, which could lead to carbon deposition.

There are only few studies regarding bimetallic catalysts for the HDO reaction [8–10]. Sun et al. [8] investigated the performance of carbon supported metal catalysts (Cu, Fe, Pd, Pt, PdFe and Ru) for HDO of guaiacol. Cyclohexanone (ONE), cyclohexanol (OL) and C₁ gas products were the main compounds formed over precious metal catalysts. On the other hand, PdFe/C catalyst exhibited higher activity to deoxygenated products (benzene/toluene) than the monometallic catalysts. DFT calculations demonstrated the preferential adsorption and activation of phenol on unreduced Fe, which likely inhibits the hydrogenation of the ring on Pd. Our group studied the selective conversion of m-cresol to toluene over bimetallic silica supported Ni-Fe catalysts [10]. For Ni/SiO₂, DFT calculations demonstrated that the aromatic compound adsorbs parallel to the surface of the metal, favoring the hydrogenation of the ring and the formation of 3-methyl-cyclohexanol and 3-methyl-cyclohexanone. For the bimetallic catalyst, the presence of an oxophilic metal, such as the unreduced Fe species present in the Ni-Fe/SiO₂ catalysts enhances the interaction with the carbonyl group. In the case of Ni-Fe [10], the DFT study shows both repulsion between the phenyl ring and the catalyst surface and a stronger interaction between the oxygen atoms in m-cresol and the catalyst surface, promoting the oxygen removal reaction pathway. In spite of few works dealing with the selectivity of bimetallic catalysts for HDO reactions, there are no studies about their deactivation.

The support also plays an important role for HDO. De Souza et al. [11–13] studied the effect of the type of support (SiO₂, Al₂O₃, TiO₂, ZrO₂, CeO₂ and CeZrO₂) on the performance of Pd-based catalysts for the hydrodeoxygenation of phenol at 573 K. Benzene was the major product over Pd/TiO₂ and Pd/ZrO₂ whereas Pd/SiO₂, Pd/Al₂O₃, Pd/CeO₂ and Pd/CeZrO₂ produced mainly cyclohexanone. For Pd/ZrO₂, the oxophilic sites represented by incompletely coordinated Zr⁴⁺ cations near the perimeter of the metal particles favor the interaction of the oxygen of the carbonyl group in the phenol tautomer intermediate with the catalyst surface. Then, the carbonyl group is preferentially hydrogenated on the metal particles at the metal-support interface, leading to the formation of benzene. Then, oxophilic supports such as zirconia promotes the production of deoxygenated products during the HDO reaction.

Therefore, the present study investigated the HDO of phenol in gas phase over bimetallic Pd catalysts (PdAg, PdZn, PdCu and PdSn) supported on ZrO₂. These elements were selected based on the literature that reports the formation of an alloy with Pd. The effect of the addition of a second metal on the catalyst activity, selectivity to deoxygenated products and stability during HDO of phenol was examined. The formation of Pd alloy with the reduction temperature was studied by *in situ* X-ray photoelectron spectroscopy (XPS) and X-ray absorption spectroscopy (XAS) experiments.

2. Experimental section

2.1. Catalyst preparation

ZrO₂ support was synthesized by the precipitation method. A solution of 2.0 mol/L zirconyl nitrate (35 wt.% ZrO(NO₃)₂ in dilute nitric acid, > 99%, Sigma-Aldrich) was added slowly to a solution of 4.0 mol/L ammonium hydroxide (NH₄OH, Vetec) at room temperature, and kept under vigorous stirring for 30 min. The resulting precipitate was filtered and washed with distilled water until a pH of 7 was reached. Then, the solid was dried in a muffle at 383 K for 12 h and calcined in a tubular reactor under dry air flow (0.2 g mL/min) at 773 K (heating ramp 5 K/min) for 6 h.

Pd/ZrO₂ catalyst was prepared by incipient wetness impregnation of the support with an aqueous solution of the Pd(NO₃)₂·xH₂O (Umicore) (wet point = 0.4 mL g⁻¹). After impregnation, the material was dried at 373 K for 12 h and then calcined in air at 673 K for 3 h (2 K min⁻¹). The bimetallic catalysts were prepared by incipient wetness co-impregnation of the support with an aqueous solution containing Pd(NO₃)₂·xH₂O and the precursors salts of the second metal (AgNO₃, Zn(NO₃)₂·6H₂O, Cu(NO₃)₂·3H₂O and SnCl₂). Then the samples were calcined following the same procedure previously described for the monometallic catalyst. All the catalysts contained 1 wt.% of Pd and a Me/Pd molar ratio of 0.5. The catalysts were designated as Pd/ZrO₂, PdAg/ZrO₂, PdZn/ZrO₂, PdCu/ZrO₂ and PdSn/ZrO₂.

2.2. Catalyst characterization

The chemical composition of each sample was determined using a Wavelength Dispersive X-Ray Fluorescence Spectrometer (WD-XRF) S8 Tiger, Bruker with a rhodium tube operated at 4 kW. The analyses were performed with the samples (300 mg) in powder form using a semi-quantitative method (QUANT-EXPRES/Bruker). BET surface areas and pore volumes of the samples were measured using a Micromeritics ASAP 2020 analyzer by nitrogen adsorption at 77 K. X-ray powder diffraction (XRD) patterns were obtained in a Rigaku equipment using CuK α radiation ($\lambda = 1.5406 \text{ \AA}$). Data were collected over the 20 range of 10° to 80° using a scan rate of 0.02°/step and a scan time of 1 s/step.

The surface properties of the catalysts were investigated by temperature-programmed desorption of ammonia (NH₃-TPD). The samples (150 mg) were reduced at 573 K for 1 h under a flow of H₂ of 60 mL/min and then purged in He flow for 30 min. After reduction, the sample was cooled to 373 K and the feed composition was switched to a mixture containing 20% NH₃ in He (30 cm³ min⁻¹) for 30 min. The physisorbed ammonia was flushed out with He flow for 1 h. Then, the catalyst was heated at 10 K/min under He to 873 K. The reactor effluent was continuously monitored by mass spectrometry.

H₂-TPR was performed in a quartz reactor coupled to a mass spectrometer (Balzers, Omnistar). Prior to a TPR experiment, each sample was pretreated under a flow of N₂ at 373 K for 1 h, and cooled to room temperature. The reducing mixture (1.96% H₂ in Ar) was passed through the sample (500 mg) and the temperature was increased to 1273 K at a heating rate of 10 K min⁻¹.

The determination of Pd particle size by transmission electron microscopy is challenging due to the low contrast between the Pd and ZrO₂ support. STEM analysis of passivated Pd/ZrO₂, PdAg/ZrO₂ and PdSn/ZrO₂ were performed and the chemical mapping of dopants and Pd was recorded. The samples were reduced at 773 K (10 K/min) in flowing H₂ (30 mL/min) for 1 h. Then, they were cooled to room temperature and passivated under a 5% O₂ in N₂ mixture (30 mL/min). The samples were analyzed with an aberration corrected Scanning Transmission Electron Microscope (STEM) (JEOL JEM-ARM200F) operated at 200 kV. The instrument is equipped with CEOS GmbH double-hexapole aberration corrector for the probe-forming lens, which allows imaging with ~0.8 nm resolution in scanning transmission electron microscopy (STEM) mode. The images were acquired on an HAADF detector with beam convergence of 27.5 mrad and collection angle of 68–280 mrad. Elemental analysis was performed using Energy Dispersive Spectroscopy (EDS) with a high collection angle SSD (~0.7 sr, JEOL Centurio). The data were acquired and evaluated with the NSSThermo Scientific software package due to the instrument upgrade. In general, the STEM sample preparation involved mounting powder samples on copper grids covered with lacey carbon support films, and then immediately loading them into the STEM airlock to minimize exposure to atmospheric O₂.

The dispersion was determined by H₂ chemisorption, using a dynamic flow method. Prior to adsorption, the sample was reduced *in situ* under pure hydrogen (30 mL/min) at 773 K for 1 h. Then, the sample was cooled to 343 K under He flow (30 mL/min). Then, pulses of 5% H₂

in Ar mixture were injected until saturation was reached, as monitored by a quadrupole mass spectrometer (Balzers, Omnistar). The adsorption was carried out at 343 K in order to avoid formation of the β -Pd hydride phase [14]. Pd dispersion was calculated assuming an H/Pd molar ratio of 1.

In order to investigate the variation of Pd dispersion during the HDO of phenol reaction, the dehydrogenation of cyclohexane reaction was used as an insensitive structure reaction to determine the Pd dispersion of the fresh and used (after HDO of phenol reaction for 24 h TOS) catalysts. This reaction was not carried out with PdCu catalyst because Cu is also active for this reaction. Therefore, the Pd dispersion was determined by a correlation between the rate of cyclohexane dehydrogenation and palladium dispersion of catalysts (Pd/SiO₂, Pd/Al₂O₃ and Pd/ZrO₂) with dispersion measured by CO chemisorption [13]. Cyclohexane dehydrogenation was performed in a fixed-bed reactor at atmospheric pressure. The fresh samples were first reduced at 773 K for 1 h and the reaction was carried out at 543 K and WHSV = 120 h⁻¹. The reaction mixture was fed into the reactor by bubbling H₂ through a saturator containing cyclohexane at 285 K (H₂/C₆H₁₂ = 13.6). At these conditions, no mass transfer or equilibrium limitations were observed. The conversions were kept below 10%. For the used catalysts, after HDO of phenol for 24 h, the saturator containing phenol was bypassed and hydrogen was allowed to flow through the catalyst for 30 min at 573 K, which removed hydrocarbons that remained adsorbed on the surface. The reactor was cooled to 543 K under hydrogen. Then, a cyclohexane/H₂ mixture was passed through the reactor. The exit gases were analyzed using an Agilent 7890 A/5975 C GCMS equipped with a HP-INNOWAX column and a flame-ionization detector (FID). The variation in dispersion after HDO of phenol reaction for 24 h of TOS was calculated according to Eq. (1), which corresponds to the ratio between the cyclohexane dehydrogenation rate of used and fresh catalysts.

$$DR(\%) = \frac{\text{Cyclohexane dehydrogenation rate of used catalyst}}{\text{Cyclohexane dehydrogenation rate of fresh catalyst}} \times 100 \quad (1)$$

XPS measurements of both unreduced as well as reduced catalysts were performed at the Environmental Molecular Sciences Laboratory facility, Pacific Northwest National laboratory in a physical Electronics Quantera Scanning X-ray Microprobe. The samples were reduced *in situ* at the different temperatures (373–773 K) under a 5%H₂/Ar mixture inside the side chamber, from which the sample can be transferred to the main spectrometer chamber without any exposure to air. After each treatment, the temperature was cooled to room temperature under 5% H₂/Ar. Then, the system was evacuated and the samples were transferred to the main chamber to proceed with the measurements. This system uses a focused monochromatic Al K α X-ray (1486.7 eV) source for excitation and a spherical section analyzer. The instrument has a 32 elements multichannel detection system. A 98 W X-ray beam focused to 100 μ m diameter was scanned over a 1.2 mm × 0.2 mm rectangle on the sample. The X-ray beam is incident normal to the sample and the photoelectron detector is at 45° off-normal. High energy resolution spectra were collected using a pass-energy of 69.0 eV with a step size of 0.125 eV. For the Ag 3d_{5/2} line, these conditions produced a FWHM of 0.91 eV. The binding energy (BE) scale is calibrated using the Cu 2p_{3/2} line at 932.62 ± 0.05 eV and Au 4f_{7/2} line at 83.96 ± 0.05 eV from known high purity reference foils. The sample experienced variable degrees of charging. Low energy electrons at ~1 eV, 20 μ A and low energy Ar⁺ ions were used to minimize this charging.

In-situ H₂-TPR XAFS studies were performed at the Materials Research Collaborative Access Team (MR-CAT) beamline at the Advanced Photon Source, Argonne National Laboratory. A cryogenically cooled Si (1 1 1) monochromator selected the incident energy and a rhodium-coated mirror rejected higher order harmonics of the fundamental beam energy. A stainless steel multi-sample holder (3.0 mm i.d. channels) was used to monitor the *in-situ* reduction of 6 samples during a single TPR run. Approximately 14 mg of each sample was

loaded as a self-supporting wafer in each channel. The catalyst to diluent weight was approximately 0.1. The holder was placed in the center of a quartz tube, equipped with gas and thermocouple ports and Kapton windows. The amount of sample used was optimized for the Pd or Ag K edge, considering the absorption by Zr of the support. The quartz tube was placed in a clamshell furnace mounted on the positioning table. Each sample cell was positioned relative to the beam by finely adjusting the position of the table to an accuracy of 20 μ m (for repeated scans). Once the sample positions were fine-tuned, the reactor was purged with helium for more than 5 min at 100 mL/min then the reactant gas (4%H₂/He) was flowed through the samples (100 mL/min) and a temperature ramp of ~1 K/min was initiated for the furnace. The sample was held at 773 K for 1 h prior to cooling to room temperature. The Pd and Ag K-edge spectra were recorded in transmission mode and a Pd metallic foil spectrum was measured simultaneously with each sample spectrum for energy calibration. X-ray absorption spectra for each sample were collected from 24,100 to 25,300 eV for Pd or 25,280 to 26,100 eV for Ag, with a step size of ~1 eV and acquisition times of 2.3 min per sample. By measuring each sample, in turn, and repeating, this allowed 37 scans to be collected for each sample over an 8.5 h period. The temperature change of the sample from the absorption edge through the end of the scan was around 2 K, while each sample was measured approximately every 13 K.

Data reduction of the EXAFS/XANES spectra was carried out using the WinXAS program [15]. The details of the XANES and EXAFS analyses are provided in previous article, and will not be repeated here, for the sake of brevity [16]. EXAFS data reduction and fitting were carried out using the catalysts in their final state following TPR and cooling using the WinXAS [15], Atoms [17], FEFF [18], and FEFFIT [19] programs. The k-range used for the fittings was 2.75–12 Å⁻¹. Fitting was confined to the first Pd-M (M = Cu, Zn, Pd, Ag, and/or Sn) or Ag-M (M = Pd and/or Ag) metallic coordination shell by applying a Hanning window in the Fourier transform magnitude spectra, and carrying out the back-transform to isolate that shell.

2.3. Activity tests

HDO of phenol was carried out in a fixed-bed quartz reactor, operating at atmospheric pressure of H₂ and 573 K. Prior to reaction, the catalyst was reduced *in situ* under pure hydrogen (60 mL/min) at 773 K for 1 h. The catalysts were diluted with inert material (m_{SiC}/m_{catal} = 3.0) to avoid the formation of hot-spots. The reactant mixture (1.6% of phenol) was obtained by flowing H₂ through the saturator containing the organic compound, which was kept at the specific temperature required to obtain the desired H₂/organic compound molar ratio (about 60). To avoid condensation, all lines were heated at 523 K. The reaction products were analyzed using an Agilent Technologies 7890 A/5975 C GCMS, using HP-Innowax capillary column and a flame-ionization detector (FID). The catalysts were evaluated at different residence time (W/F) by varying the catalyst amount in the range of 2.5–200 mg. The W/F is defined as the ratio of catalyst mass (g) to organic feed mass flow rate (g/h). The stability tests were performed during 24 h of time on stream (TOS), using W/F value corresponding to the highest phenol conversion obtained.

The product yield and selectivity for each product were calculated as follows (Eqs. (2) and (3)):

$$\text{Yield}(\%) = \frac{\text{mol of product produced}}{\text{mol of phenol fed}} \times 100 \quad (2)$$

$$\text{Selectivity}(\%) = \frac{\text{mol of product produced}}{\text{mol of phenol consumed}} \times 100 \quad (3)$$

The stability of the catalysts was defined as the ratio between the reaction rate at t₀ = 0.2 h and t_f = 24 h TOS (Eq. (4)), assuming that the deactivation rate exhibits a first-order kinetics.

Table 1

BET surface area, pore volume, pore size, Pd and dopant content of the samples and Pd dispersion determined by H₂ chemisorption and by cyclohexane dehydrogenation.

Samples	Pd (wt%)	Dopant/Pd ^a	BET area (m ² g ⁻¹)	Pore Volume (cm ³ g ⁻¹)	Dispersion ^b (%)	Dispersion ^c (%)
Pd/ZrO ₂	1.02	—	77	0.30	35	38
PdAg/ZrO ₂	0.98	0.49	73	0.29	11	9
PdCu/ZrO ₂	0.97	0.55	79	0.30	6	—
PdSn/ZrO ₂	0.97	0.30	79	0.28	9	10
PdZn/ZrO ₂	1.00	0.55	76	0.29	4	5

^a Molar ratio.

^b Measured by hydrogen chemisorption.

^c Measured by cyclohexane dehydrogenation reaction.

$$DP = \frac{\ln(1 - X_{end})}{\ln(1 - X_{initial})} \quad (4)$$

3. Results and discussion

3.1. Catalyst characterization

Table 1 shows the Pd loadings and dopant/metal molar ratios of the catalysts. Pd content was close to the nominal value (1 wt%) for all samples. The samples exhibited a dopant/Pd molar ratio around the expected value (0.50), except for PdSn/ZrO₂ that was slightly lower (0.30). **Table 1** also presents the textural properties of the catalysts. All samples showed similar specific surface areas (73–79 m² g⁻¹), which are close to the surface area of the support (82 m²/g). The total pore volumes (0.28–0.30 cm³ g⁻¹) were also very similar for all the catalysts. The addition of small amount of Pd and the other metals did not change the specific surface area and pore volume of the samples.

X-ray diffraction patterns of the calcined samples are compared in Fig. S1 (Supporting information). The diffractograms of all samples showed lines characteristic of a mixture of monoclinic (JCPDS 37-1484) and tetragonal (JCPDS 17-0923) ZrO₂ phases. The proportion of each phase was calculated taking into account the procedure proposed by Khaodee et al. [20]. The monoclinic is the dominant phase for all catalysts, varying from 82 to 88%. The lines characteristic of palladium and transition metals oxides were not detected. This is likely due to the low content of these metals.

The NH₃-TPD profiles of all zirconia supported catalysts are shown in the Supplementary Information section (Fig. S2). Only one broad peak is observed in the TPD profile with a maximum located between 500–550 K. de Souza et al. [13] carried out NH₃-TPD for Pd supported over zirconia with different structures (tetragonal, monoclinic and mixtures). They also observed a similar TPD profile for all Pd-based catalysts. DRIFTS of adsorbed pyridine showed bands of pyridine adsorbed on Lewis acid sites represented by unsaturated Zr⁴⁺ cations. Therefore, the NH₃-TPD profiles in our work indicates the presence of Lewis acid sites on all catalysts.

Pd dispersion of fresh catalysts measured by H₂ chemisorption and cyclohexane dehydrogenation reaction are also reported in **Table 1**. The results obtained by both techniques were quite close, revealing that the cyclohexane dehydrogenation reaction can be used for the determination of metal dispersion. Furthermore, these techniques showed a decrease in Pd dispersion when the second metal was added. Considering that H₂ chemisorption occurs only on Pd surface, these results might be explained by one or more of the following reasons [21]: (i) sintering of Pd particles by the addition of second metal; (ii) the formation of an alloy between Pd-second metal, which may modify the adsorption properties of Pd atoms; (iii) the second metal partially covers the surface of Pd particle (ensemble effect).

In order to investigate the effect of the addition of a second element on the metal particle size, STEM analysis was carried out. The STEM images of the Pd/ZrO₂ catalyst are shown in Fig. S3 (Supporting information). Due to the low Pd content and the poor contrast between Pd

and ZrO₂, it is difficult to distinguish between the Pd particles and the individual ZrO₂ crystallites in the STEM image shown in Fig. S3. Therefore, the size distribution analysis was not performed. Only few Pd particles were found with 2.5 nm. The same problem happens with PdAg/ZrO₂ and PdSn/ZrO₂ catalysts but the few particles observed have approximately the same size (2.5 nm) compared to that of the monometallic catalyst. Therefore, sintering of Pd particles due to the addition of the second element on the bimetallic catalysts could be ruled out.

These results are not in agreement with the metal dispersion determined by H₂ chemisorption as well as cyclohexane dehydrogenation reaction, which estimated larger metal particles for the bimetallic catalysts. As the chemisorption and the probe reaction are indirect measurements of dispersion, this decrease is likely due to the alloy formation or the coverage of the Pd surface by the second metal.

The formation of an alloy between Pd-second metal was studied by TPR, in situ EXAFS, in situ XPS and the results obtained will be discussed next.

3.2. Effect of the second metal on Pd reduction and alloy formation

Fig. 1 shows the TPR profiles obtained for zirconia-supported catalysts. For Pd/ZrO₂, the reduction profile exhibits one peak at 430 K and a shoulder at around 500 K. The hydrogen consumption at this low temperature region is attributed to the reduction of palladium oxide with different particle sizes [22]. There is also a hydrogen uptake at high temperature (650–750 K). The hydrogen uptake obtained in the low temperature region corresponds exactly to the complete reduction of PdO (**Table 2**). Therefore, the H₂ consumption at high temperature (650–750 K) could be attributed to the reduction of zirconia support. The XANES spectra at the Zr K-edge of Pd/ZrO₂ catalysts after reduction at different temperatures showed that Zr⁴⁺ was partially reduced to Zr³⁺, which is in agreement with the result of our TPR profile [13].

TPR profiles of bimetallic catalysts are similar to that of Pd/ZrO₂,

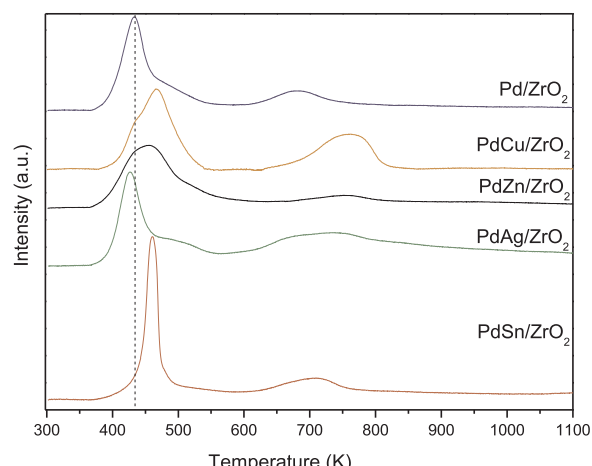


Fig. 1. TPR profiles of Pd and bimetallic supported on zirconia catalysts.

Table 2

H_2 consumption related to the 1st and 2nd peaks in the TPR profile and the degree of PdO reduction.

Samples	H_2 observed consumption in the 1 st Peak (mol g ⁻¹) × 10 ^{5a}	H_2 observed consumption in the 2 nd Peak (mol g ⁻¹) × 10 ⁵	Total consumption × 10 ⁵	Expected Consumption of dopant (mol/g) × 10 ^{5b}	Expected total consumption (mol/g) × 10 ^{5b}	PdO degree of reduction 1 st peak (%)	Total reduction degree (%) (dopant + Pd)
Pd/ZrO ₂	4.74	2.76	7.50	—	4.72	100	159
PdAg/ZrO ₂	4.84	7.41	12.2	2.27	6.99	103	175
PdCu/ZrO ₂	5.27	3.41	8.68	4.33	9.04	112	96
PdSn/ZrO ₂	7.10	4.46	11.6	2.53	7.24	151	160
PdZn/ZrO ₂	4.46	3.63	8.09	4.21	8.92	95	91

^a Expected H_2 consumption for total reduction of PdO (4.71×10^{-5} mol g⁻¹).

^b Expected H_2 consumption considering total reduction of SnO₂, CuO, Ag₂O and ZnO.

with the main reduction peak around 400–550 K and a second peak at high temperature. An additional peak relative to the dopant metal reduction did not appear in any of the bimetallic profiles. In general, this result may be attributed to the formation of an alloy. Fox et al. [23] also observed that the reduction occurred in a single broad peak for PdCu/CeO₂ bimetallic catalyst. Karski et al. [22] reported similar results for the following bimetallic systems: 5%Pd–1%Ag/SiO₂, 5%Pd–3%Ag/SiO₂ ad 5%Pd–5% Ag/SiO₂. According to them, this corresponds to the reduction of a Pd_xAg_yO mixed oxide formed during the calcination with oxygen. Vicente et al. [14] showed that PdO is completely reduced around 373 K for 1%Pd/SiO₂. The TPR profile of Pd-Sn/SiO₂(1%Pd-1-2%Sn) bimetallic catalysts exhibited the reduction of Sn species in contact with Pd, which may be an indication of alloy formation. In our work, hydrogen consumption observed between 400–550 K corresponds to the complete reduction of PdO for PdAg/ZrO₂, PdCu/ZrO₂ and PdZn/ZrO₂, indicating that only Pd oxide is reduced in the low temperature region (Table 2). Ag₂O, CuO and ZnO were completely reduced in the high temperature region. For PdSn/ZrO₂, the hydrogen uptake in the first peak is higher than that expected for the reduction of PdO, which suggests that Sn oxide is also reduced in this region. The higher total hydrogen consumption observed for Pd/ZrO₂, PdAg/ZrO₂ and PdSn/ZrO₂ indicates that ZrO₂ is also partially reduced at this temperature, as reported by de Souza et al. [13].

TPR-XANES spectra as a function of temperature are shown in Fig. 2 and snapshots of XANES spectra at the initial, intermediate, and final stages of reduction are provided in Fig. 3.

The temperatures to achieve 50% of PdO reduction were as follows for the various catalysts according to edge energy: Pd K-edge: Pd (372 K); Pd-Cu (370 K); Pd-Zn (346 K); Pd-Ag (360 K); Pd-Sn (374 K). Thus, significant promoting effects on reduction were observed by adding Zn or Ag to the Pd particles. The slightly lower temperature of Ag compared to Pd in the Pd-Ag catalyst suggests that nucleation of reduced metal centers in the Pd-Ag catalyst occurred at Ag atoms. Once the Ag° centers were formed, Pd was rapidly reduced (temperature difference at 50% metal reduction for Ag and Pd are within 1.3 K). Then, a significant fraction of Ag is likely in intimate contact with Pd, and quite possibly at the atomic level (e.g., alloy formation). This effect can be clearly observed in Fig. 3.

The evolution of the Pd species during reduction calculated by the linear combination of Pd K-edge XANES spectra is shown in Fig. 4. The initial spectrum of the oxidized catalyst and the final spectrum of the reduced catalyst were used as references for the linear combination fittings. The calcined samples contain PdO and the reduction to Pd° begins at around 333 K for all samples. The temperature to achieve 90% as metallic Pd was 418 K for Pd; 419 K for Pd-Cu; 372 K for Pd-Zn; 394 K for Pd-Ag; and 404 K for Pd-Sn, while the temperature was 385 K to achieve 90% as metallic Ag for the Pd-Ag catalyst.

TPR-EXAFS spectra as a function of temperature are shown in Fig. 5. Snapshots of EXAFS spectra at the initial, intermediate, and final stages of reduction are provided in Fig. 6. In agreement with the TPR-XANES results, the initial spectra (Fig. 5, spectrum at room temp) are

dominated by the Pd-O bond. The EXAFS spectra following reduction at ~773 K for Pd, Pd-Ag, and Pd-Sn catalysts are dominated by a single peak located between 2 and 3 angstroms in the phase-uncorrected Fourier transform magnitude spectra, which can be assigned to the first Pd-Pd shell [24]. On the other hand, the EXAFS spectra of Pd-Cu and Pd-Zn catalysts show two peaks, one located close to 2 angstroms and the second peak, though smaller in magnitude as compared to Pd, Pd-Ag, and Pd-Sn catalysts, situated between 2 and 3 angstroms. XRD studies indicate that doping of Cu [25] or Zn [26] to Pd should lead to a decrease in the lattice spacing, while doping of Ag [27] or Sn [28] should lead to a slight increase in lattice spacing.

The raw $\chi(k)$ spectra presented in Fig. 7 reveal that there are only slight differences in the spectra of Pd-Ag (Fig. 7g) and Pd-Sn (Fig. 7p) compared to the Pd alone catalyst (Fig. 7d). There is a sharpening of the fifth maxima and an increase in the sixth minima. The result shows subtle differences in higher shells (~5 angstroms) in the Fourier transform magnitude spectra. Thus, the results are suggestive of alloying for all the samples. The oscillations are significantly attenuated due to interference phenomena in the raw $\chi(k)$ spectra of Pd-Cu (Fig. 7m) and Pd-Zn (Fig. 7s) catalysts as compared to Pd alone (Fig. 7d). In addition, two clearly defined peaks emerge in the FT magnitude spectra of Pd-Cu (Fig. 7o) and Pd-Zn (Fig. 7u) catalysts as compared to Pd alone (Fig. 7f), consistent with the presence of both Pd-Pd and Pd-Cu or Pd-Zn in the first coordination sphere.

EXAFS fitting parameters of all catalysts, as well as that of the Pd foil reference are given in Table 3. For the case of the Pd-Ag catalyst, two different fittings were conducted; a fitting where data were treated separately at the Pd and Ag K-edges, and a fitting whereby some shared parameters were utilized in the fitting (e.g., Pd-Ag distance). The coordination number of the first Pd-Pd shell for Pd/ZrO₂ determined by curve-fitting was 8.6 (Pd-Pd distance, 2.733 Å). The bimetallic samples showed total coordination numbers slightly higher than that of the monometallic catalyst, except for PdZn (PdAg (9.5); PdCu (10.0); PdSn (9.2); and PdZn (6.3)). The average coordination number is the EXAFS parameter related to the size and shape of the metal particles and then, it can be used to provide a rough estimate of the particle size using the analysis of Jentys [29]. Assuming a fcc crystal structure, spherical cluster morphology, and similar atomic radii relative to Pt (e.g., Cu – 135 pm, Zn – 135 pm, Sn – 145 pm, Pd – 140 pm, Pt – 35 pm, Ag – 160 pm), the results suggest that Pd/ZrO₂ catalyst had a cluster size of 1.8 ± 0.3 nm, while the PdAg, PdCu, and PdSn bimetallic catalysts exhibited slightly larger sizes (2.8 ± 0.9 nm, 3.3 ± 1.0 nm, 2.4 ± 0.9 nm), and the PdZn catalyst had a slightly smaller size (1.0 ± 0.4 nm).

Moreover, the local atomic concentration of palladium in the bimetallic catalysts was calculated by the $N_1/(N_1 + N_2)$ ratio: PdAg (67%); PdCu (67%); PdSn (77%); and PdZn (68%). The results obtained indicate that the first shell around Pd atoms is close to the chemical composition expected for the bimetallic catalysts.

For Pd-Cu and Pd-Zn catalysts, the fitting parameters floated to distances consistent with virtually complete alloying, since these

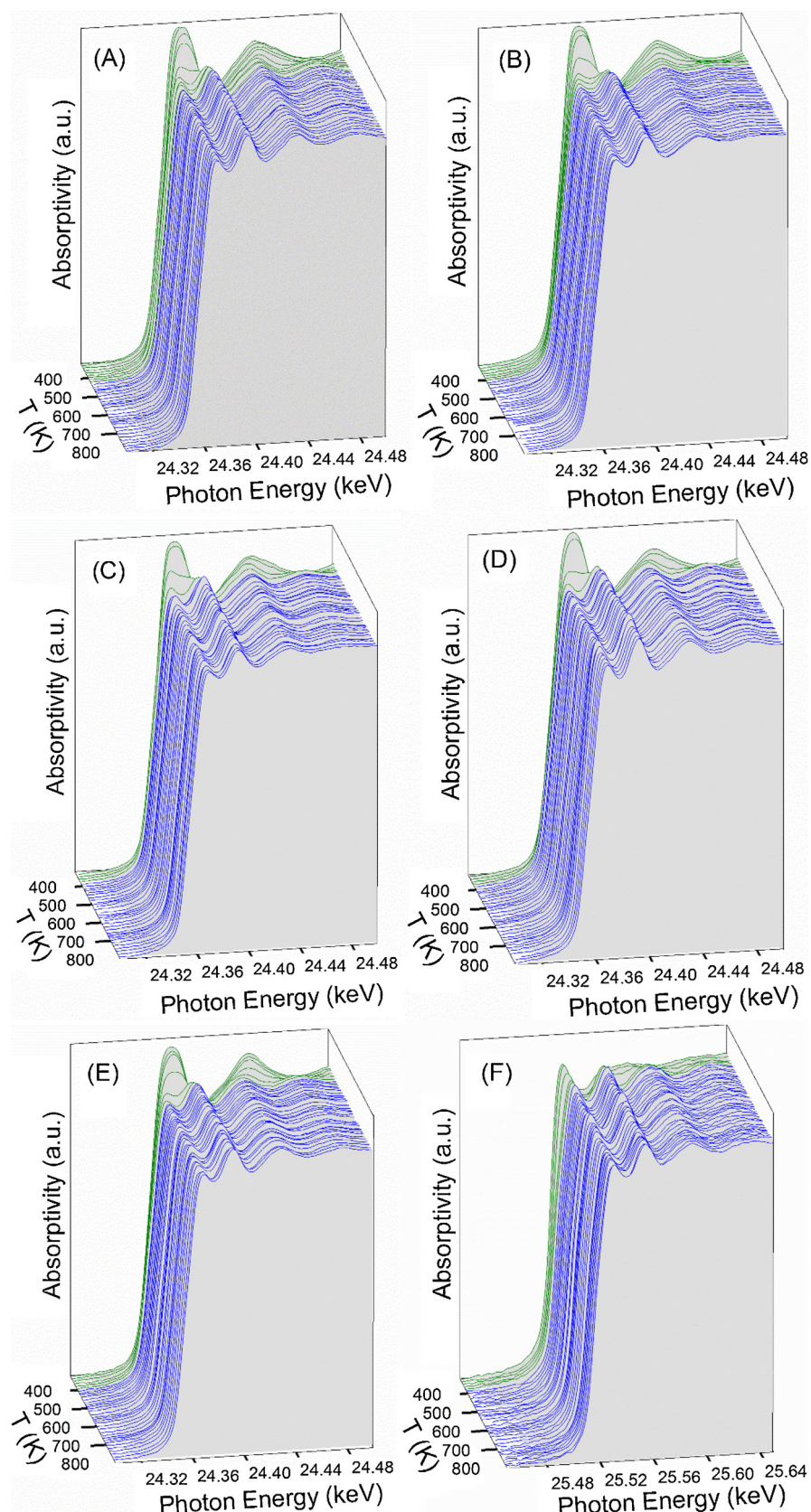


Fig. 2. Hydrogen TPR-XANES profiles at the Pd K-edge of (A) Pd, (B) Pd-Cu, (C) Pd-Zn, (D) Pd-Ag, and (E) Pd-Sn catalysts as a function of temperature.

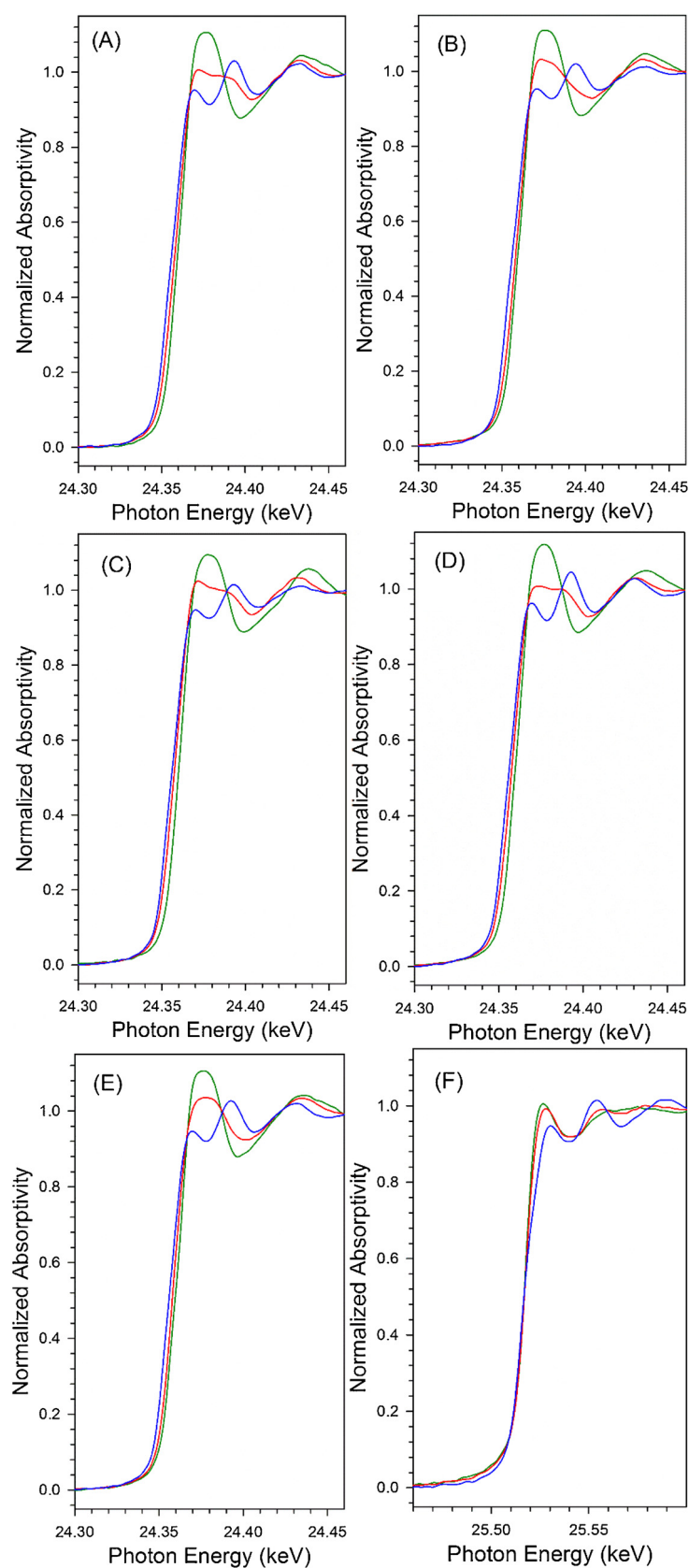


Fig. 3. Snapshots of XANES profiles at the Pd K-edge at (green line) ~331 K; (red line) partial reduction; and (blue line) ~773 K complete reduction of (A) Pd; (B) PdCu; (C) PdZn; (D) PdAg; and (E) PdSn catalysts, and at the Ag K-edge of (F) PdAg catalyst (For interpretation of the references to color in this figure legend, the reader is referred to the web version of this article).

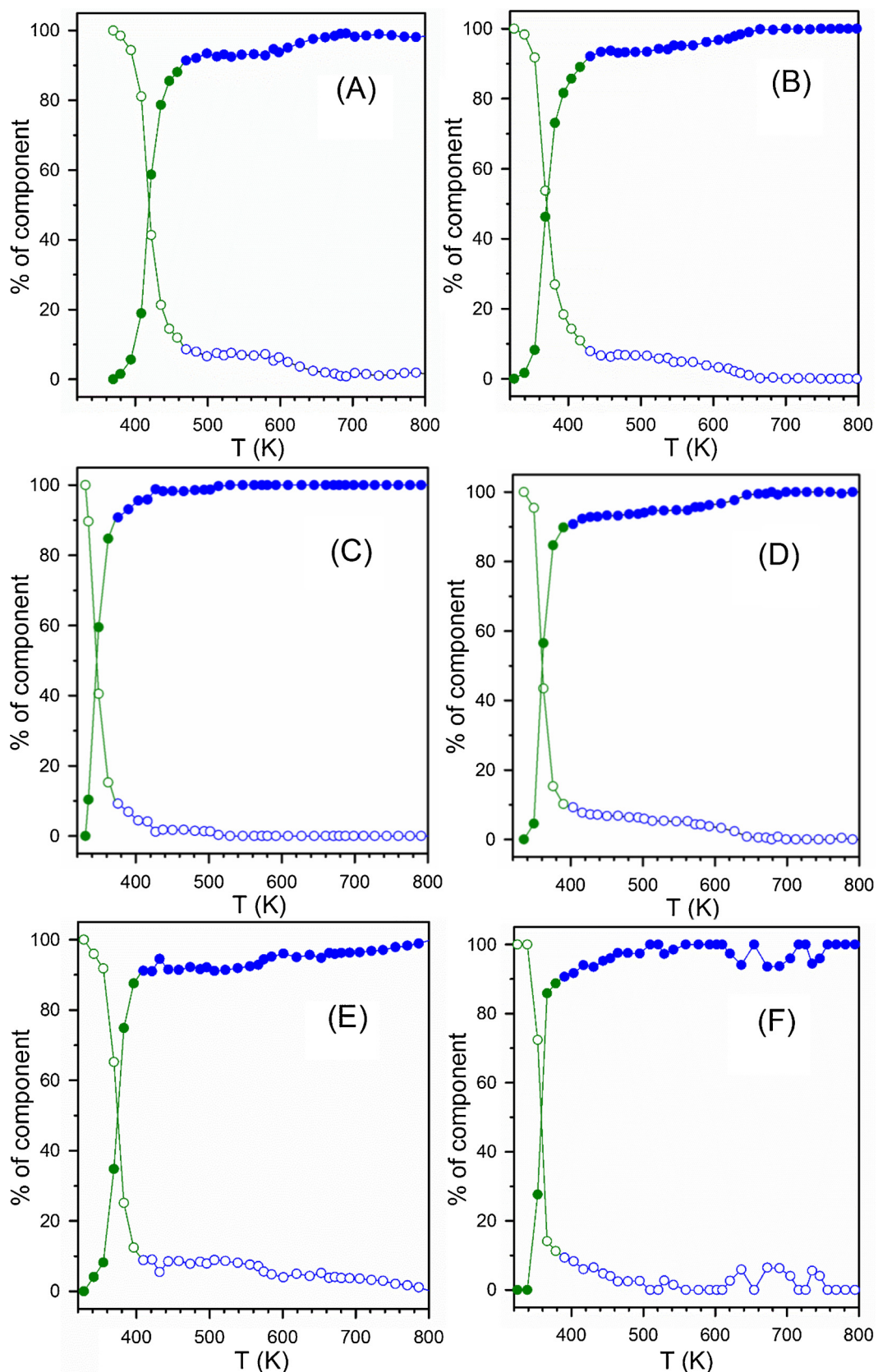


Fig. 4. Linear combination fittings of TPR-XANES profiles at the Pd K-edge of (A) Pd, (B) Pd-Cu, (C) Pd-Zn, (D) Pd-Ag, and (E) Pd-Sn catalysts, and (F) at the Ag K-edge of Pd-Ag. (Green) % metallic < 90%; (Blue) % metallic greater than or equal to 90% (For interpretation of the references to color in this figure legend, the reader is referred to the web version of this article).

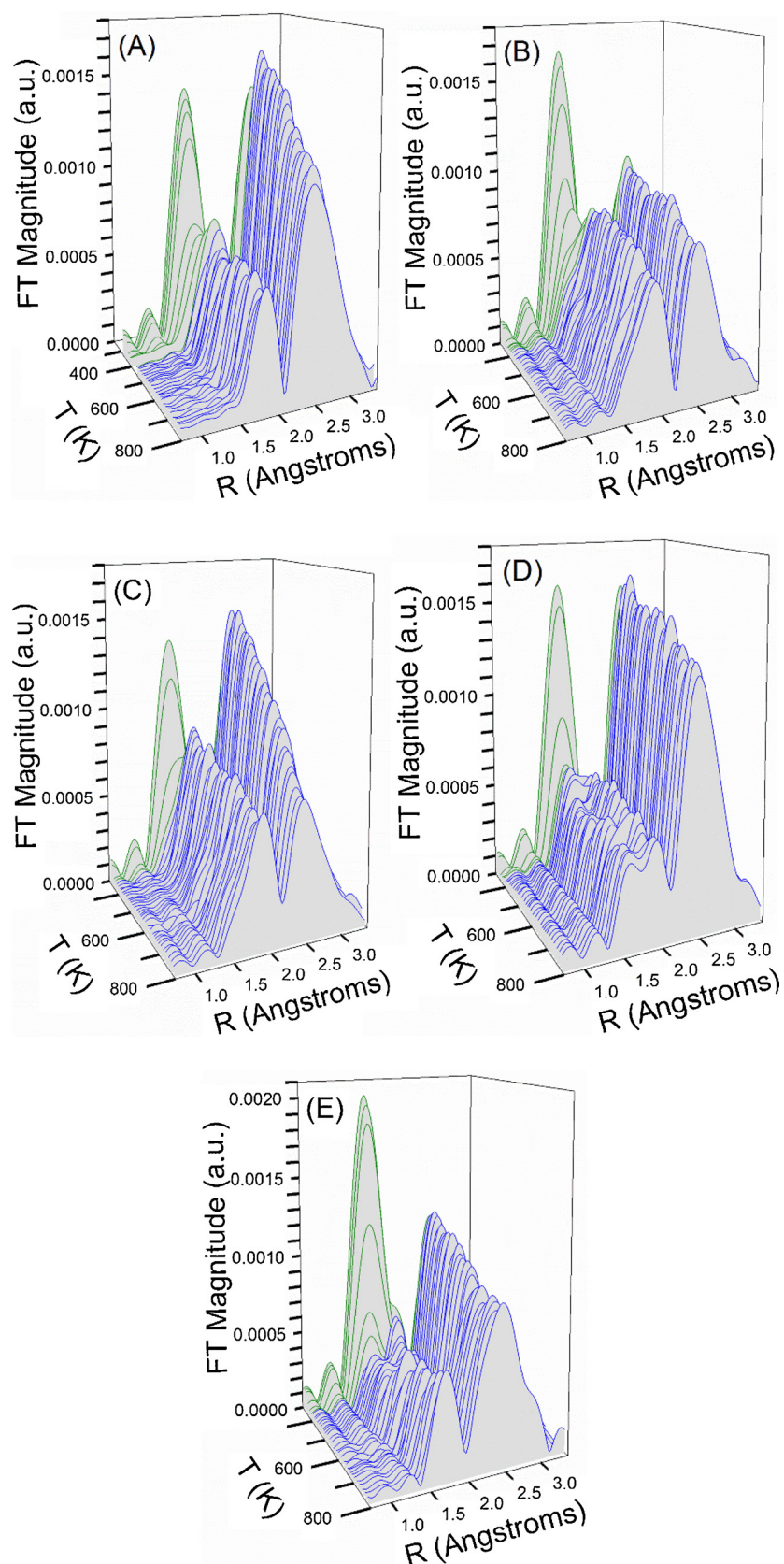


Fig. 5. Hydrogen TPR-EXAFS k^1 -weighted Fourier transform magnitude spectra at the Pd K-edge of (A) Pd, (B) Pd-Cu, (C) Pd-Zn, (D) Pd-Ag, and (E) Pd-Sn.

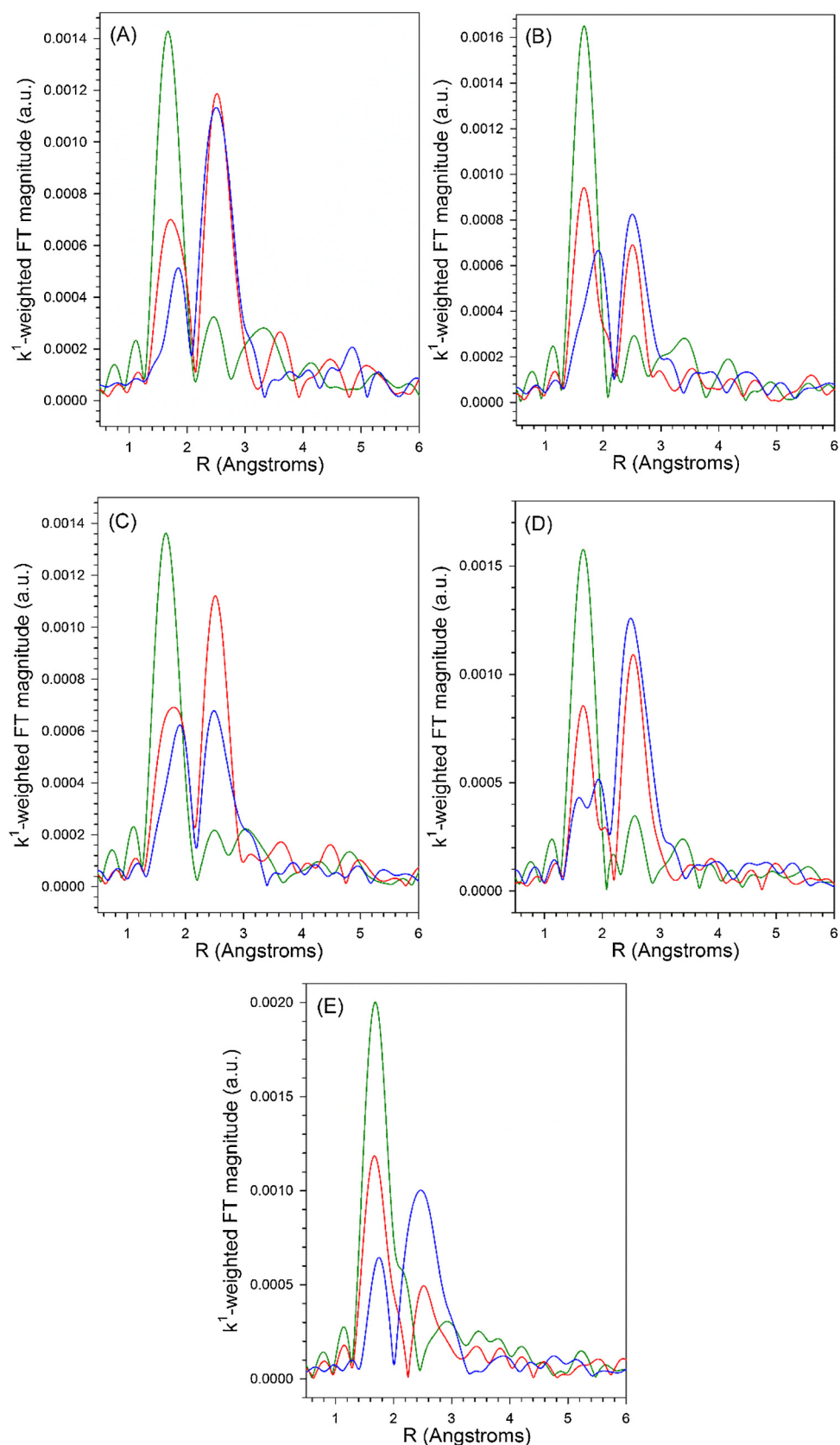


Fig. 6. Snapshots of EXAFS profiles at the Pd K-edge at (green line) ~ 331 K; (red line) partial reduction; and (blue line) ~ 773 K complete reduction of (A) Pd; (B) PdCu; (C) PdZn; (D) PdAg; and (E) PdSn catalysts. (For interpretation of the references to color in this figure legend, the reader is referred to the web version of this article).

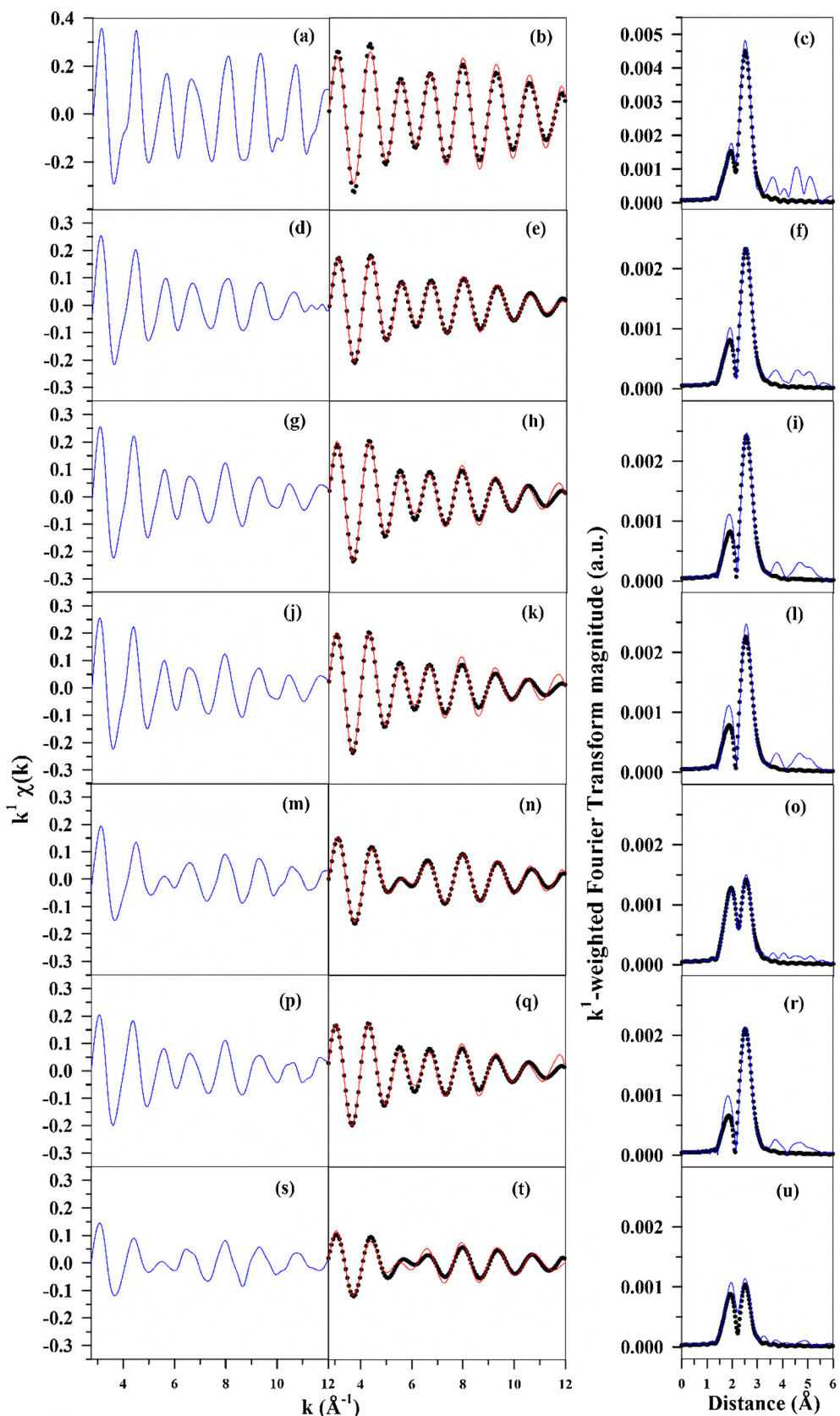


Fig. 7. (left) (blue line) raw k^1 -weighted $\chi(k)$ spectra; (middle) (solid red line) filtered and (filled circles) fitted k^1 -weighted $\chi(k)$ spectra; and (right) (solid blue line) raw and (filled circles) fitted k^1 -weighted Fourier Transform magnitude spectra of (a–c) Pd^o foil and (d–f) Pd, (g–i) Pd-Ag (separate fitting), (j–l) Pd-Ag (combination fitting), (m–o) Pd-Cu, (p–r) Pd-Sn, and (s–u) Pd-Zn catalysts. Fittings were conducted over the first Pd-M (M=Pd and/or Ag, Cu, Sn, Zn) coordination shell (For interpretation of the references to color in this figure legend, the reader is referred to the web version of this article).

Table 3

Results of EXAFS fitting parameters for references acquired near the Pd K-edge. The fitting ranges were $\Delta k = 2.75\text{--}12.0 \text{\AA}^{-1}$ and $\Delta R = 1.5\text{--}3.0 \text{\AA}$. $S_0^2 = 0.9$.

Sample	N_1 Pd-Pd	R Pd-Pd (\AA)	N_2 Pd-M ^a	R Pd-M ^a (\AA)	e_0 (eV)	$\sigma^2 (\text{\AA}^2)$	r-factor
Pd'foil	12 (set)	2.739 (0.0078)	—	—	-1.69 (0.53)	0.00635 (0.00061)	0.014
Pd/ZrO ₂	8.6 (0.30)	2.733 (0.0048)	—	—	-1.67 (0.28)	0.00951 (0.00064)	0.0022
PdAg/ZrO ₂ separate fitting ^b	6.4 (0.46)	2.727 (0.010)	3.1 (0.23)	2.798 (0.011)	-2.37 (0.58)	0.00913 (0.0014)	0.0080
PdAg/ZrO ₂ combined fitting	6.8 (2.8)	2.724 (0.018)	3.3 (2.3)	2.794 (0.018)	-2.65 (0.52)	0.0105 (0.0015)	0.012
PdCu/ZrO ₂	6.7 (0.35)	2.701 (0.0070)	3.3 (0.36)	2.604 (0.0067)	-3.29 (0.47)	0.0102 (0.00091)	0.0045
PdSn/ZrO ₂ ^b	7.1 (0.63)	2.723 (0.012)	2.1 (0.19)	2.765 (0.013)	-1.87 (0.71)	0.0103 (0.0017)	0.012
PdZn/ZrO ₂	4.3 (0.71)	2.683 (0.026)	2.0 (0.67)	2.615 (0.024)	-4.94 (1.33)	0.00787 (0.0038)	0.018

Sample	N Ag-Ag	R Ag-Ag (\AA)	N Ag-Pd	R Ag-Pd (\AA)	e_0 (eV)	$\sigma^2 (\text{\AA}^2)$	r-factor
PdAg/ZrO ₂ separate fitting ^b	2.9 (0.14)	2.818 (0.0077)	5.9 (0.28)	2.749 (0.0075)	-0.867 (0.380)	0.0128 (0.0011)	0.0026
PdAg/ZrO ₂ combined fitting	0.0 (1.4)	2.864 (0.019)	7.8 (1.3)	2.794 (0.018)	-2.65 (0.52)	0.0105 (0.0015)	0.012

^a Where M = Ag, Cu, Sn, or Zn.

^b Where M (Ag or Sn) and Pd were partitioned according to the molar ratio in the first coordination shell.

samples showed a shorter Pd bond distance (Pd-Cu- 2.701 Å; Pd-Zn- 2.681 Å versus 2.733 Å for the monometallic sample). Similar results were observed by Fox et al. [23] in an EXAFS analysis of 30% Cu-1% Pd/CeO₂ and 30% Cu-1% Pd/Al₂O₃ and it was associated with alloy formation. The r-factor for the Pd (0.0022) and PdCu fitting were excellent (0.0045), while that of PdZn was good (0.018). For both PdAg (separate fitting) and PdSn, an attempt to fit the data without constraints led to nonsensical values, where Pd-M (M=Ag and Sn) distances were significantly shorter than Pd-Pd distances. The r-factors for the separate fittings of PdAg and PdSn were excellent (0.0026) and good (0.012), respectively. In those cases, constrained fittings were made where Pd and Ag or Sn were partitioned according to their molar ratio in the first coordination shell. In that case, the results were consistent with alloy formation.

Pd and Ag have a similar backscattering amplitude and phase effects on the photoelectron wave, which makes it hard to distinguish the parameters between these two elements. However, the near-neighbor distances of Pd and Ag are quite different: Pd-Pd (2.75 Å) and Ag-Ag (2.88 Å) [30]. Thus, to better evaluate alloy formation in Pd-Ag systems some authors conducted EXAFS analysis at both metal edges [31]. TPR-EXAFS spectra and the EXAFS profiles at different points of the reduction process for Ag K-edge data corresponding to the Pd-Ag catalyst are provided in Fig. S4 (Supporting information). The EXAFS spectrum at room temperature shows a distinct peak for Ag-O coordination, while following reduction, a significant asymmetric peak is formed between 2 and 3 angstroms consistent with Ag-M coordination, where M is Ag and/or Pd. EXAFS fittings at the Ag K-edge are shown in Fig. S5 (Ag K-edge), while the EXAFS fittings in the Pd K-edge are shown in Fig. 7. The fitting parameters are presented in Table 3. For Pd-Ag catalyst, two different fittings were conducted, a fitting where data were treated separately at the Pd and Ag K-edges, and a fitting whereby some shared parameters were utilized in the fitting (e.g., Pd-Ag distance). After this modification, the obtained results were consistent with alloy formation. With the combination fitting for PdAg, the results suggest that Ag is, for the most part, surrounded by Pd, while Pd is surrounded by both Pd and Ag in the first coordination shell, with the ratio being consistent with alloy formation. The r-factors for the PdAg combination fitting was also good (0.012).

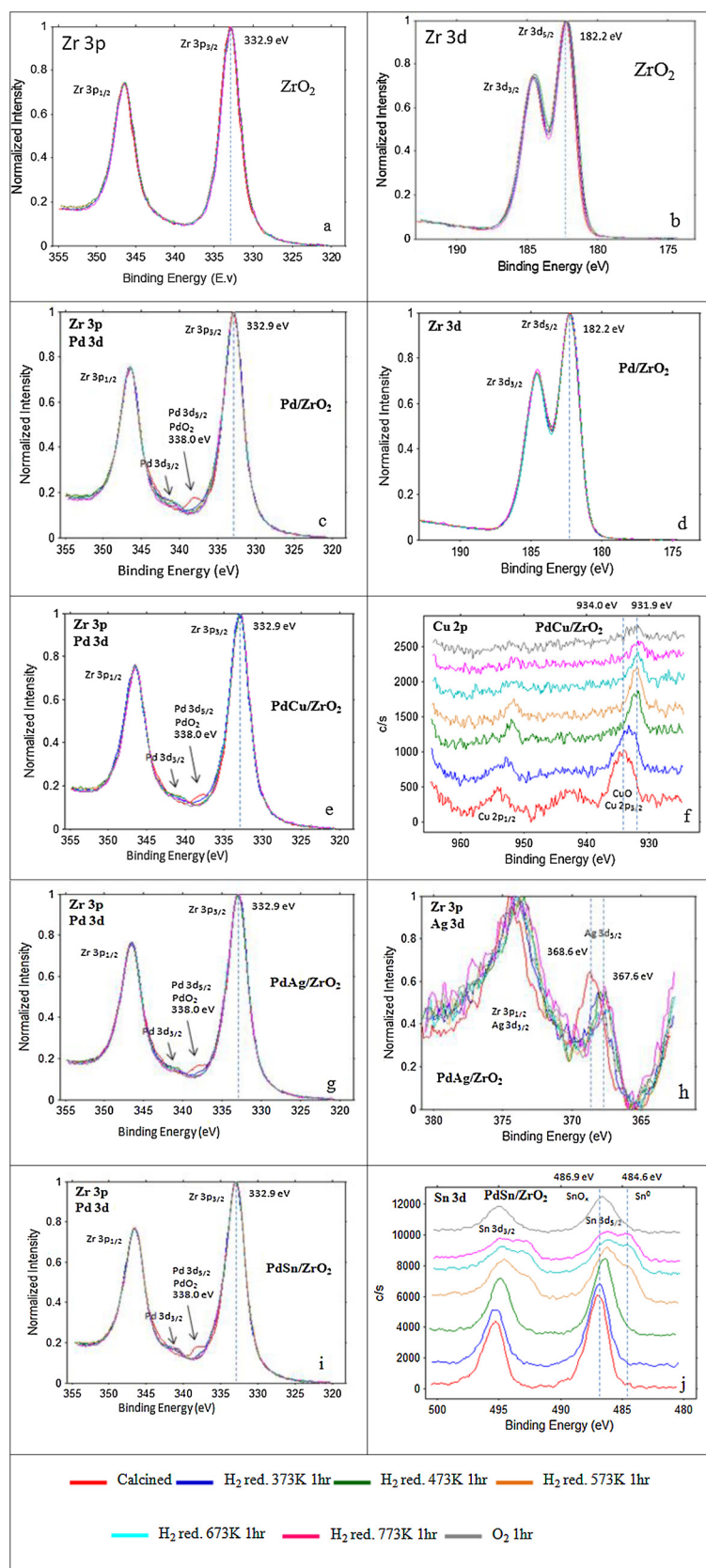
XPS experiments were carried out at different reduction temperatures in order to follow the evolution of the surface composition (Fig. 8). Fig. 8a and b shows the Zr 3p and Zr3d spectra, respectively. All catalysts exhibited a spin-orbit doublet of the Zr3d core level into 3d_{5/2} and 3d_{3/2} levels with an energy gap of 2.4 eV between them (Fig. 8d) as well as a doublet of the Zr3p core level representing 3p_{1/2} and 3p_{3/2}. This suggests the existence of ZrO₂-like species according to previous data in the literature [32]. The analysis of the Pd 3d spectra is

rather complicated due to the overlapping with the more intense Zr 3p doublet [32–34], which hinders the identification of metallic palladium. The Pd 3d spectrum of the calcined Pd/ZrO₂ sample displays a shoulder at around 338.0 eV that corresponds to the binding energy (B.E.) of Pd3d_{5/2} of PdO₂ [35]. However, the data treatment of the spectrum by subtraction of the Zr 3p spectra of the support in order to obtain the Pd 3d spectrum was not carried out due to the low signal-to-noise ratio. The same problem was reported by Faticanti et al. [32] for the XPS analyses of Pd/ZrO₂ catalysts containing 0.9 and 1.1 wt.% Pd. The reduction at 373 K led to the disappearance of this peak and the appearance of a shoulder corresponding to the B.E. of Pd3d_{3/2}, indicating that PdO was reduced to Pd°. After reduction at 773 K, the samples were submitted to an oxidative atmosphere (pure O₂) at room temperature, but the Pd° particles were stable against re-oxidation.

The Cu 2p spectra of PdCu/ZrO₂ are shown in Fig. 8f. The calcined sample exhibits a peak around 934.8 eV, which is characteristic of Cu²⁺ species in CuO [36]. After reduction at 373 K, a rather asymmetric peak is observed, with a shoulder at 934.8 eV, indicating that partial reduction of CuO takes place. Further increasing to 473 K produces a peak around 931.9 eV, which is assigned to Cu° [23]. This result suggests that copper was completely reduced at this temperature [36]. Increasing the reduction temperature to 773 K decreased the intensity of this band that is likely due to Cu° sintering. According to the literature, the Cu 2p peak related to Cu° in this work is shifted towards lower BE around 0.9 eV²³. Fox et al. [23] observed that for CuPd/CeO₂ bimetallic catalysts the Cu 2p_{3/2} and Cu2p_{1/2} peaks were located at 932.0 and 951.6 eV, respectively, which were shifted by 0.4–0.6 eV compared to the monometallic Cu/CeO₂ catalyst. These results may be an indication of the existence of a PdCu alloy.

For PdAg/ZrO₂ (Fig. 8h), the spectrum for the calcined sample exhibited a band around 368.6 eV. After reduction at 373 K, this band moved to 367.6 eV and remained unchanged during heating up to 773 K. According to the literature, the binding energy of Ag⁺ in Ag₂O is around 367.8 eV, while the value around 368.2 eV indicates the presence of metallic Ag [37]. Therefore, this result revealed the presence of Ag° on the PdAg/ZrO₂ calcined sample. The B.E. of Ag 3d_{5/2} observed for the reduced sample was shifted -0.6 eV in comparison to the binding energy of Ag°, which suggests the formation of a Pd-Ag alloy. The core level shifts relative to pure Pd and Ag depend on changes in the bulk charge around an atomic site. According to Lamb et al. [38], the partial charge transfer from Ag to Pd during the reduction treatment can result in a decrease in the binding energy of Ag.

Fig. 8j displays the Sn 3d spectra of PdSn/ZrO₂ catalyst. The spectrum of the calcined sample showed two peaks at 486.8 eV and 495.3 eV attributed to the Sn 3d_{5/2} and 3d_{3/2} core levels respectively. According to the literature [14,39,40], these peaks correspond to the

Fig. 8. XP spectra of the Pd/ZrO_2 and PdMe/ZrO_2 catalysts ($\text{Me}=\text{Ag, Cu and Sn}$).

presence of oxidized Sn. However, it is not possible to distinguish between Sn^{2+} and/or Sn^{4+} oxidation states through XPS analysis [14,41]. According to Nishiiyama et al. [41], the spectra of SnO_2 powder and Sn foil showed peaks at 486.9 and 484.8 eV, respectively, which were assigned to Sn^{2+} and/or Sn^{4+} species and Sn° . The spectrum remained unchanged after reduction at 373 K. The treatment at 473 K under H_2 slightly shifted the bands to lower binding energies, indicating that tin oxide is partially reduced to species with lower valence. The increase in the reduction temperature to 573 K led to the appearance of a shoulder at 484.6 eV, which suggests that metallic tin was formed. This result is in agreement with the TPR experiment that also revealed the reduction of tin oxide around this temperature. The spectrum obtained after reduction at 773 K still contains the peaks characteristic of SnO and Sn° , which reveals that tin remains partially oxidized on the surface at this temperature.

In general, palladium is known to form an homogenous solid solution at all compositions with different metals, such as Ag [42,43], and Cu [44,45]. Fernández-García et al. [46] studied the reduction of three Pd-Cu/KL-zeolite bimetallic catalysts with different Pd:Cu atomic ratios. This study was performed using XANES and infrared spectroscopy of adsorbed CO as a probe molecule. The authors observed the formation of Pd-Cu alloys, with electronic perturbation of both components over the full range of compositions. According to them, the alloy particles did not exhibit significant Cu segregation on the surface. Venezia et al. [47] studied the structure of supported Pd-Ag and Pd-Cu catalysts. The samples were characterized by XPS and XRD. In general, the systems showed different behaviors; For Pd-Cu, it was observed a mixture of monometallic and alloyed particles, while silver segregation to the surface was observed with no evidence of alloy formation for Pd-Ag. Cárdenas et al. [48] used chemisorption technique to investigate the Pd_nSn_m alloys in PdSn supported samples. For the samples supported on Al_2O_3 a relatively small amount of Sn alloying with Pd was observed. However, Sn apparently tends to cover the Pd particles on the silica supported catalysts. Vicente et al. [14] confirmed the existence Pd-Sn bimetallic interactions for PdSn/ SiO_2 . According to them, the quantity of Sn° species suggested the formation of a Pd_3Sn alloy for samples reduced above 573 K. The formation of PdZn alloy has also been reported in the literature [49,50]. The bulk PdZn alloy was formed by the spill-over of atomic hydrogen from the Pd metal to the ZnO , leading to facile reduction of the ZnO and migration of Zn to the metallic surface [51]. It is important to note that it was not possible to determine the surface composition of the samples by XPS analysis. The Pd 3d signal derived from spectra subtraction had a too low signal-to-noise ratio to lead to unambiguous results.

3.3. HDO of phenol

The phenol conversion and product yield for HDO of phenol at 573 K over all catalysts as a function of W/F are shown in Fig. 9.

The zirconia support was also tested and it was inactive under the reaction conditions used. Pd/ ZrO_2 catalyst was much more active than all bimetallic catalysts. The addition of metal dopant decreased the phenol conversion, as the W/F range used for the bimetallic samples was higher. This agrees very well with the decrease in H_2 chemisorption and reaction rate of cyclohexane dehydrogenation reaction.

The product distributions showed a remarkable dependence on the type of the second metal. For Pd/ ZrO_2 catalyst, benzene was the dominant product for $\text{W/F} > 0.1$ h, with the formation of cyclohexanone (ONE) and traces amounts of C_{12} hydrocarbons (biphenyl, cyclohexylbenzene) and C_{12} oxygenated compounds (2-phenylphenol, 2-cyclohexylphenol, 2-cyclohexylcyclohexan-1-one). de Souza et al. [12] showed that the formation of these bicyclic compounds during the HDO of phenol comes from the alkylation of phenolic and aromatic rings by cyclohexanone, which is catalyzed by Lewis acid sites. The presence of the Lewis acid sites on the Pd and Pd-Metal/ ZrO_2 catalysts was determined by NH_3 -TPD experiments.

PdCu/ ZrO_2 catalyst showed a product distribution similar to that observed for Pd/ ZrO_2 . However, significant formation of benzene was achieved only at higher W/F (> 0.5 h). Cyclohexanone was the main product over PdZn/ ZrO_2 catalyst. The other products formed were benzene and C_{12} oxygenated compounds, with small amounts of cyclohexanol. The addition of Ag to Pd promoted the formation of cyclohexanone, decreasing the production of benzene. Furthermore, a higher formation of C_{12} hydrocarbons and C_{12} oxygenated compounds was also observed. PdSn/ ZrO_2 catalyst exhibited similar product distribution of the monometallic catalyst, with higher formation of C_{12} oxygenated compounds.

Fig. S6 (Supporting information) displays the selectivity as a function of conversion. For all catalysts, increasing the phenol conversion rises the selectivity to benzene and bicyclic compounds, whereas the formation of cyclohexanone decreases.

The reaction rate of HDO of phenol was calculated and the selectivity of all catalysts was compared at low phenol conversion (around 13%), as shown in Table 4. The monometallic catalyst showed the highest reaction rate that followed the order: Pd > PdAg ≈ PdCu > PdSn > PdZn. Therefore, the addition of the second element decreased the reaction rate, in direct correlation with the decreases in site density as measured by H_2 chemisorption and cyclohexane dehydrogenation rate. Taking into account that STEM images did not reveal a growth in the metal particles due to the addition of the second metal and that EXAFS experiments indicated the formation of Pd alloy, the decrease in the phenol reaction rate suggests that Pd particles are covered by the metal dopant or the Pd-alloy has a lower activity. Pd/ ZrO_2 exhibited the highest selectivity to benzene followed by PdSn, while the addition of Ag, Cu and Zn favors the formation of cyclohexanone and cyclohexanol. These results indicate that the type of metal dopant significantly impacts the adsorptive and catalytic properties of Pd particles, which is likely due to the formation of Pd-based alloys.

3.4. The effect of the second metal on the reaction pathways for HDO of phenol

Different catalysts have been studied for HDO of phenolic compounds such as phenol or cresol, including supported noble metals (Pd, Pt, Rh, Ru) [6,9,11,52–58] supported base metals (Ni, Co, Fe, Cu) [3,5,6,59–63] and bimetallic catalysts [10,8]. However, studies comparing the performance of a series of catalysts with different metals are scarce and only few were carried out in gas phase but in these cases, the HDO of m-cresol was investigated [10].

Studies were performed about the HDO of m-cresol in gas phase at 573 K over different silica supported catalysts (Pd, Pt, Ru, Ni, Fe, NiFe) [64,65]. Hydrogenation products (3-methylcyclohexanone and 3-methylcyclohexanol) were the main products formed over Pt/ SiO_2 , Pd/ SiO_2 and Ni/ SiO_2 catalysts, whereas toluene was the dominant product on Fe and Ni-Fe bimetallic catalysts. Ru/ SiO_2 catalyst showed significant formation of toluene as well as CH_4 and $\text{C}_2\text{-C}_6$ hydrocarbons. For the bimetallic catalyst, the presence of an oxophilic metal, such as the unreduced Fe species promoted the hydrogenation of the carbonyl group of the tautomer intermediate, producing toluene.

Sun et al. [8] investigated the performance of different supported metal catalysts (Cu/C, Fe/C, Pd/C, Pt/C, PdFe/C, and Ru/C) for the vapor phase hydrodeoxygenation of guaiacol at 523–723 K temperature range. For all the samples, phenol was the major intermediate product. For the noble metals, the main reaction pathway was the saturation of the aromatic ring, which leads to the formation of cyclohexanone and cyclohexanol. The base metals showed lower activity than the noble metal catalysts, however they favored the formation of ring-saturated or ring-opening products. The bimetallic PdFe/C catalyst showed the highest HDO activity and selectivity to deoxygenated products.

In the present work, Pd/ ZrO_2 catalyst exhibited the highest selectivity to benzene. The high selectivity to deoxygenated products of zirconia supported catalysts has been attributed to the presence of

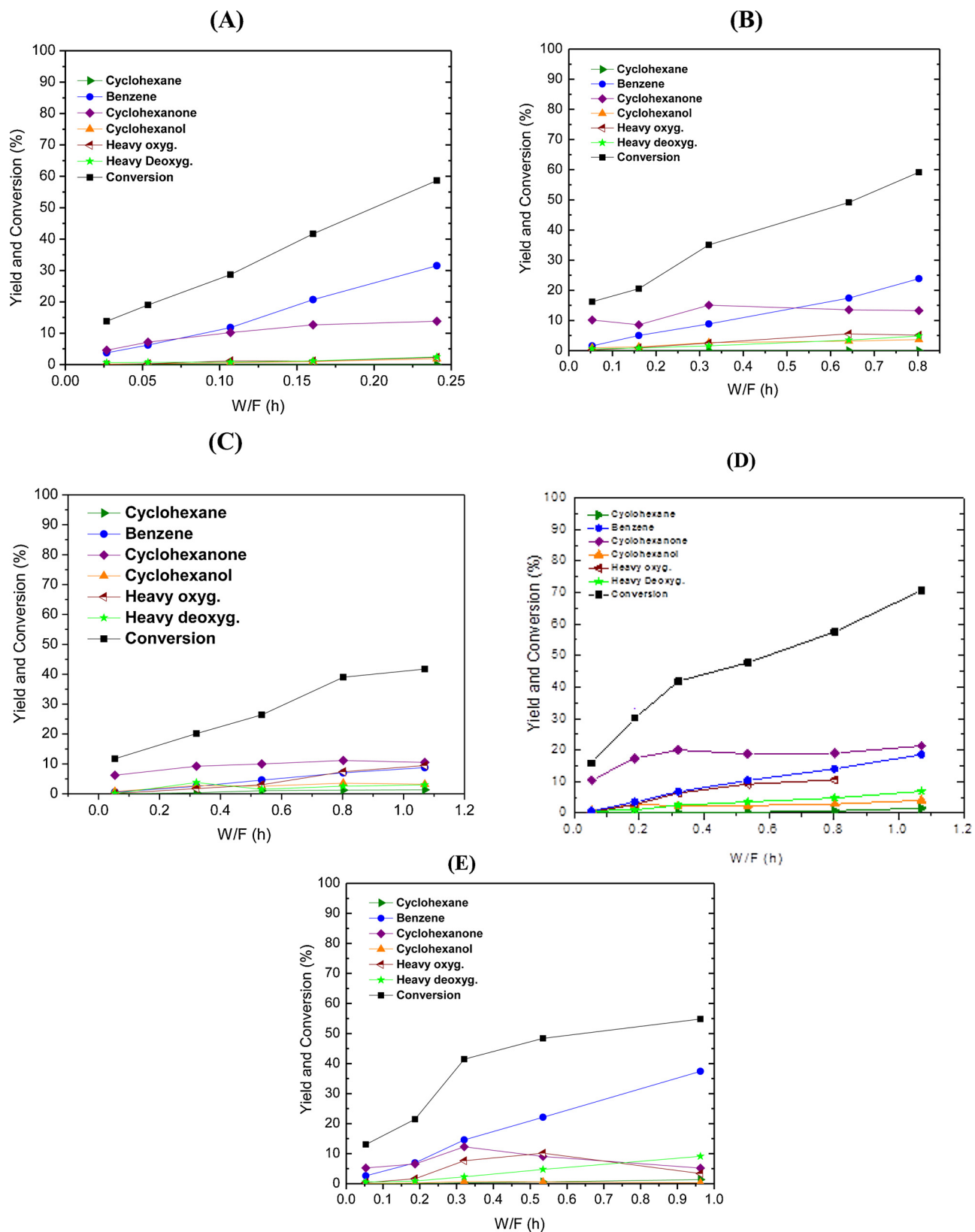


Fig. 9. Phenol conversion and yield of products as a function of W/F over: (A) Pd/ZrO₂; (B) PdCu/ZrO₂; (C) PdZn/ZrO₂; (D) PdAg/ZrO₂; (E) PdSn/ZrO₂. Reaction conditions: T = 573 K, P = 1 atm, and H₂/phenol molar ratio = 60.

oxophilic sites represented by incompletely coordinated Zr⁴⁺ and Zr³⁺ cations near the perimeter of the metal particles [11]. These oxophilic sites favor the interaction of the oxygen of the carbonyl group in phenol tautomer intermediate with the metal particle. Then, the carbonyl

group is preferentially hydrogenated on the metal particles at the metal-support interface, leading to the formation of benzene after the facile dehydration of the reactive intermediate. However, the addition of a second metal significantly affected product distribution for HDO of

Table 4

Conversion, selectivity and reaction rate for HDO of phenol at 573 K and atmospheric pressure.

Samples	Conversion (%)	Selectivity (%)					Reaction Rate (mol _{phenol} min ⁻¹ g _{cat} ⁻¹)
		Benzene	OL	ONE	C ₁₂ Oxigenated	C ₁₂ Hydrocarbon	
Pd/ZrO ₂	9.09	41.29	1.58	50.34	0.0	6.78	0.086
PdAg/ZrO ₂	12.99	4.97	6.32	80.70	2.68	5.34	0.049
PdCu/ZrO ₂	13.54	11.79	7.15	74.91	1.68	4.46	0.050
PdSn/ZrO ₂	8.91	29.29	1.28	58.96	4.03	6.43	0.040
PdZn/ZrO ₂	7.74	7.51	9.57	80.36	1.24	1.32	0.036

phenol over Pd/ZrO₂ catalyst. The following order of selectivity to cyclohexanone and cyclohexanol was observed: Pd (52%) < PdSn (60%) < PdCu (82%) < PdAg (87%) ≈ PdZn (90%). Considering the reaction mechanism based on the tautomerization, Ag, Cu and Zn dopants seem to promote the hydrogenation of the ring, producing preferentially cyclohexanone and cyclohexanol. Sn exhibits an intermediate behavior, closer to the monometallic Pd catalyst, which favored the formation of benzene likely due to the hydrogenation of the carbonyl group. Therefore, the hydrogenation capacity of Pd was enhanced in the presence of Ag, Cu and Zn dopants, suggesting that adsorptive and catalytic properties of Pd were modified. In our work, in situ EXAFS and XPS provided evidence for the formation of Pd alloy with the second element for all these samples (Pd-Ag; Pd-Cu and Pd-Zn), which could be responsible for the increase in the hydrogenation capacity observed.

Iwasa et al. [66] studied the hydrogenation of crotonaldehyde over supported Pd catalysts in gas phase. The authors showed that alloying of Pd with Zn improves the activity for hydrogenation of crotonaldehyde to crotyl alcohol. According to the authors, the selectivity to unsaturated alcohol is improved when the Pd is alloyed with another more electropositive metal, which increases the electron density of the Pd and favors the hydrogenation of the C=O. Sitthisa et al. [67] reported that the incorporation of Cu to Pd/SiO₂ catalyst results in the formation of PdCu alloys, which exhibited an electronic structure different from that of pure Pd. This electronic change affects the product distribution of the hydrogenation of furfural and 2-methylpentanal. The overall activity and the decarbonylation selectivity for both reactions decreased on PdCu catalysts, while the selectivity to hydrogenation and etherification increased.

Therefore, in this work, the interaction of the oxygen of the carbonyl group from the phenol tautomer intermediate with the Pd surface is likely weakened, favoring the hydrogenation of the ring due to the Pd alloying with Ag, Cu, and Zn dopants.

However, PdSn/ZrO₂ catalyst showed a higher formation of benzene than the other bimetallic catalysts. In fact, XPS analysis of PdSn sample revealed the presence of unalloyed Sn that remained as tin oxide on the surface even after reduction at high temperature. Once Snⁿ⁺ is located at or near the hydrogenation active metal particles, it favors the adsorption of the reagent through its carbonyl group, which increases the hydrogenation probability of the C=O double bond. The same result was reported by Nie et al. [10] for a NiFe/SiO₂ catalyst where the unreduced Fe species promoted the hydrogenation of the carbonyl group. Vicente et al. [14] studied the influence of the structural properties of the PdSn/SiO₂ catalysts on citral hydrogenation reaction. According to them, the addition of Sn considerably increases the selectivity towards the unsaturated alcohol. These results were attributed to the formation of the Pd₃Sn intermetallic phase.

Regardless of the type of the dopant, C₁₂ hydrocarbons (biphenyl, cyclohexylbenzene) and C₁₂ oxygenated compounds (2-phenylphenol, 2-cyclohexylphenol, 2-cyclohexylcyclohexan-1-one) were also observed. These bicyclic hydrocarbons have been observed during the conversion of HDO of phenol over Pd/Al₂O₃, whereas only trace amounts of these compounds were detected over Pd/ZrO₂ [11]. Bicyclic products are formed by the alkylation of phenolic and aromatic rings by

cyclohexanone. Alkylation is catalyzed by acid sites such as Lewis acid sites present on the supports. The formation of Pd alloy with the second element increased the hydrogenation capacity of Pd, increasing the selectivity to cyclohexanone for all bimetallic catalysts. Therefore, the higher formation of bicyclic compounds on the Pd-Me/ZrO₂ catalysts is likely due to the higher production of cyclohexanone, which favors the alkylation reaction over the Lewis acid sites present on zirconia.

The variation of product distribution could also be attributed to the changes in ensemble size. In this work, Pd dispersion significantly decreased when the metal dopant was added (Table 1). De Souza et al. [11] studied the effect of Pd particle size on the product distribution for HDO of phenol over Pd/ZrO₂ catalysts, which had different Pd dispersions. Both catalysts exhibited similar selectivities indicating that metal dispersion does not significantly affect the product distribution for HDO of phenol reaction.

In our work, the decrease in the HDO reaction rate and the changes in product selectivities were likely due to the alloy formation and surface segregation.

3.5. Stability tests

Phenol conversion and product distributions as a function of TOS (24 h) for all catalysts are shown in Fig. 10.

Pd/ZrO₂, PdCu/ZrO₂, PdSn/ZrO₂ and PdAg/ZrO₂ showed similar initial conversion (60%), while PdZn/ZrO₂ had lower initial conversion (40%) (Fig. 10a). All catalysts deactivated mainly during the first 6 h of TOS but the deactivation degree depended on the type of the metal. The stability of the catalysts defined by Eq. (4) was calculated and the results are listed in Table 5 (deactivation parameter – DP). Pd/ZrO₂, PdZn/ZrO₂ and PdAg/ZrO₂ exhibited approximately the same deactivation degree. These results demonstrate that the addition of these dopants did not decrease catalyst deactivation during HDO of phenol. Therefore, the Pd-alloying with Ag, Zn and Cu did not have a positive effect on catalyst stability. However, the loss in activity was less pronounced for PdSn/ZrO₂ catalyst.

There were also changes in the product distribution along the reaction (Fig. 10b–f). Selectivity to cyclohexanone and benzene remained approximately constant during 24 h for all catalysts. However, the selectivity to C₁₂ oxygenated compounds (2-phenylphenol, 2-cyclohexylphenol, 2-cyclohexylcyclohexan-1-one) significantly increased whereas the C₁₂ hydrocarbons (biphenyl, cyclohexylbenzene) were no longer detected after 6 h of TOS.

Catalyst deactivation is one of the main challenges of HDO reactions. Catalyst deactivation during HDO of phenol could be due to the sintering of the metallic particles, changes in the density of acid sites or the deposition of carbonaceous species on the catalyst surface [3]. In order to investigate the main causes of deactivation of Pd-dopant/ZrO₂, the spent catalysts were characterized by Raman spectroscopy and cyclohexane dehydrogenation reaction. The Raman spectra of the used catalysts did not show bands characteristic of carbon materials in the range of 1200–1800 cm⁻¹. This result indicates that the deactivation of Pd catalysts was likely not caused by the coverage of Pd particles or acid sites by carbonaceous deposits.

The comparison between the rates of the cyclohexane

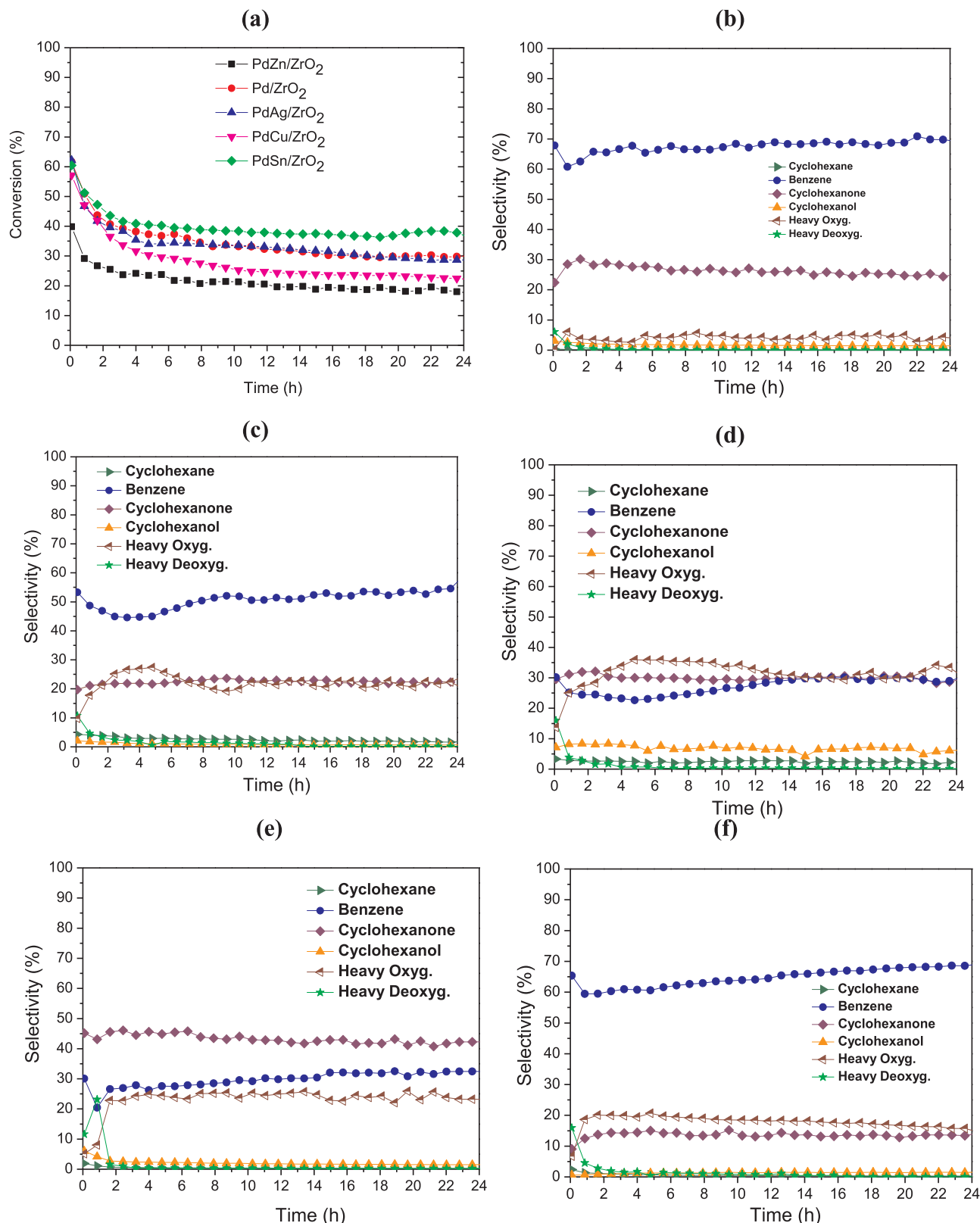


Fig. 10. Conversion of phenol (A) and selectivity to products as a function of TOS for: (B) Pd/ZrO₂ ($W/F = 0.320 \text{ h}^{-1}$); (C) PdCu/ZrO₂ ($W/F = 0.963 \text{ h}^{-1}$); (D) PdZn/ZrO₂ ($W/F = 1.069 \text{ h}^{-1}$); (E) PdAg/ZrO₂ ($W/F = 0.963 \text{ h}^{-1}$); (F) PdSn/ZrO₂ ($W/F = 0.963 \text{ h}^{-1}$). Reaction conditions: $T = 573 \text{ K}$, $P = 1 \text{ atm}$, and H₂/phenol molar ratio = 60.

dehydrogenation reaction before and after HDO of phenol was used to provide information about changes in Pd particle size during HDO reaction. Table 6 lists the Pd dispersion of the fresh and used catalysts after 24 h of TOS. This experiment was not carried out with PdCu

catalyst because Cu is also active for this reaction. Pd dispersion significantly decreased during the reaction, indicating that the sintering of Pd particles is one of the causes for catalyst deactivation. The undoped Pd catalyst exhibited the highest decrease in the ratio of the reaction

Table 5
Deactivation parameters (DP) of the studied samples.

Samples	X _{initial}	X _{final}	DP
Pd/ZrO ₂	0.62	0.30	0.37
PdAg/ZrO ₂	0.62	0.28	0.34
PdCu/ZrO ₂	0.57	0.22	0.29
PdSn/ZrO ₂	0.60	0.36	0.49
PdZn/ZrO ₂	0.39	0.16	0.35

rate of cyclohexane dehydrogenation of the used and fresh catalyst (DR), whereas the lowest decrease was observed for PdSn/ZrO₂ catalyst. These results are in agreement with deactivation observed during HDO of phenol reaction (Table 5), confirming that Pd sintering is the main cause of catalyst deactivation. Furthermore, the addition of dopants (Ag, Zn) to Pd/ZrO₂ did not improve the resistance of Pd to sintering and then, the catalysts still deactivated in spite of the formation of a Pd-alloy.

Changes in the density of acid sites of the support may also contribute to catalyst deactivation. However, in our work, all samples use the same support and then, it is expected that the changes in the density of acid sites will affect all the samples in a similar way and could not explain the differences in deactivation observed among the catalysts.

Recently, de Souza et al. [12] investigated the mechanism of deactivation of Pd-based catalysts for HDO of phenol. All catalysts deactivated during the reaction but the deactivation degree depended on the support. Pd/ZrO₂ catalyst showed a strong deactivation during the reaction. The DRIFTS experiments revealed that there was a significant buildup of intermediate species on the surface during the reaction. This result was attributed to the loss of the metal-support interface due to the growth of Pd particles that affects the ability of the adsorbed species to turnover, leading to an accumulation of phenoxy species during reaction.

Therefore, metal sintering is likely the main cause of the deactivation of zirconia supported bimetallic catalysts of the present work. Among the samples, PdSn/ZrO₂ showed a deactivation ratio lower than the others, however it had a similar metal sintering level. The higher stability observed for this sample may be related to the presence of Sn oxide on its surface as revealed by XPS analysis. Snⁿ⁺ species are oxophilic sites that favors the adsorption of the keto-tautomer of phenol through its carbonyl group and promotes the hydrogenation of the C=O bond. These sites turn over the oxygenate intermediates, decreasing their accumulation on the surface and reducing catalyst deactivation.

Metal sintering also affected the product distribution. The selectivity to C₁₂ oxygenated compounds significantly increased as a function of TOS. Therefore, the reactions that take place at the metal-support interface were inhibited, whereas the reactions on the Lewis acid site remained less affected, leading to an increase in the selectivity to C₁₂ oxygenated compounds.

4. Conclusions

This work studied the performance of zirconia supported bimetallic catalysts for HDO of phenol reaction. Pd/ZrO₂ catalyst exhibited the highest activity and selectivity to benzene. This has been attributed to the presence of oxophilic sites represented by Zr⁴⁺ and Zr³⁺ cations near the perimeter of the metal particles, which favors the interaction of the oxygen from the carbonyl group of phenol tautomer intermediate with the metal particle. Then, the carbonyl group is preferentially hydrogenated on the metal particles at the metal-support interface, leading to the formation of benzene after the facile dehydration of the reactive intermediate.

The addition of a second metal significantly affected activity and product distribution for HDO of phenol over Pd/ZrO₂ catalyst. All bimetallic catalysts exhibited lower reaction rates for HDO of phenol compared to the monometallic one. H₂ chemisorption, the reaction of dehydrogenation of cyclohexane, STEM and EXAFS demonstrated that the loss in activity was due to the surface segregation of the second metal or the formation of Pd alloy, respectively. The following order of selectivity to cyclohexanone and cyclohexanol was observed: Pd < PdSn < PdCu < PdAg ≈ PdZn. Considering the reaction mechanism based on the tautomerization, Ag, Cu and Zn dopants seem to promote the hydrogenation of the ring, producing preferentially cyclohexanone and cyclohexanol. Sn exhibits an intermediate behavior, closer to that of the monometallic Pd catalyst, with a higher formation of benzene, which is likely due to the hydrogenation of the carbonyl group.

Therefore, the hydrogenation capacity of Pd was enhanced in the presence of Ag, Cu and Zn dopants, suggesting that adsorptive and catalytic properties of Pd were modified. In situ EXAFS, STEM and XPS provided evidence for the formation of Pd alloy with the second element for all the samples, which could be responsible for the increase in the hydrogenation capacity observed.

XPS analysis of PdSn sample revealed the presence of unalloyed Sn that remained as tin oxide on the surface even after reduction at high temperature. For the PdSn/ZrO₂ catalyst, tin oxide should exhibit an oxophilicity that promoted the formation of benzene. Once Snⁿ⁺ is located at or near the metal particles, it favors the adsorption of the keto-tautomer of phenol through its carbonyl group, which increases hydrogenation of the C=O bond.

All catalysts deactivated mainly during the first 6 h of TOS. Pd/ZrO₂ and PdZn/ZrO₂ and PdAg/ZrO₂ exhibited approximately the same deactivation degree. However, the loss of activity was less pronounced for PdSn/ZrO₂ catalyst. The Raman spectra of the used catalysts did not show bands characteristic of carbon materials in the range of 1200–1800 cm⁻¹. The comparison between the rates of the cyclohexane dehydrogenation reaction before and after HDO of phenol was used to provide information about changes in Pd particle size during HDO reaction. Pd dispersion significantly decreased during the reaction, indicating that the sintering of Pd particles is one of the causes for catalyst deactivation.

Table 6
Reaction rate of cyclohexane dehydrogenation reaction and calculated dispersion by dehydrogenation of cyclohexane before and after HDO of phenol reaction.

Samples	Fresh catalyst		Used catalyst		DR (%) ^b
	Reaction rate ^a	Dispersion (%)	Reaction rate ^a	Dispersion (%)	
Pd/ZrO ₂	7.78E-04	38	1.23E-04	7	15.8
PdAg/ZrO ₂	1.84E-04	9	1.57E-05	1	8.5
PdCu/ZrO ₂	7.02E-04	—	1.57E-05	—	—
PdSn/ZrO ₂	2.10E-04	10	1.26E-05	1	6.0
PdZn/ZrO ₂	9.32E-05	5	1.28E-05	1	13.7

^a mol cyclohexane/(g_{Pd} min).

^b Eq. 1.

Acknowledgments

The authors thank CAPES (Coordenação de Aperfeiçoamento de Pessoal de Ensino Superior) and CNPq (Conselho Nacional de Desenvolvimento Científico e Tecnológico) for supporting this research and the scholarship received. The XPS and TEM analyses were performed by Drs. Mark Engelhard and Libor Kovarik, respectively, using resources at EMSL, a DOE Office of Science User Facility sponsored by the Office of Biological and Environmental Research and located at Pacific Northwest National Laboratory. The work carried out at the CAER was supported in part by funding from the Commonwealth of Kentucky. Argonne's research was supported in part by the U.S. Department of Energy (DOE), Office of Fossil Energy, National Energy Technology Laboratory (NETL). The use of the Advanced Photon Source was supported by the U.S. Department of Energy, Office of Science, Office of Basic Energy Sciences, under Contract No. DE-AC02-06CH11357. MRCAT operations are supported by the Department of Energy and the MRCAT member institutions.

Appendix A. Supplementary data

Supplementary data associated with this article can be found, in the online version, at <https://doi.org/10.1016/j.apcatb.2018.03.041>.

References

- [1] G.W. Huber, J.A. Dumesic, *Catal. Today* 111 (2006) 119–132.
- [2] A.V. Bridgwater, *Appl. Catal. A* 116 (1994) 5–47.
- [3] P.M. Mortensen, J.D. Grunwaldt, P.A. Jensen, A.D. Jensen, *ACS Catal.* 3 (2013) 1774–1785.
- [4] A.V. Bridgwater, *Biomass Bioenergy* 38 (2012) 68–94.
- [5] E. Furimsky, *Appl. Catal. A* 199 (2000) 147–190.
- [6] T.V. Choudhary, C.B. Phillips, *Appl. Catal. A* 397 (2011) 1–12.
- [7] I. Graça, J.M. Lopes, H.S. Cerqueira, M.F. Ribeiro, *Ind. Eng. Chem. Res.* 52 (2013) 275–287.
- [8] J. Sun, A.M. Karim, H. Zhang, L. Kovarik, X.S. Li, A.J. Hensley, J.S. Mc Ewen, Y. Wang, *J. Catal.* 306 (2013) 47–57.
- [9] Y. Hong, H. Zhang, J. Sun, K.M. Ayman, A.J.R. Hensley, M. Gu, M.H. Engelhard, J.S. Mc Ewen, Y. Wang, *ACS Catal.* 4 (2014) 3335–3345.
- [10] L. Nie, P.M. de Souza, F.B. Noronha, W. An, T. Sooknoi, D.E. Resasco, *J. Mol. Catal. A Chem.* 388 (2014) 47–55.
- [11] P.M. de Souza, R.C. Rabelo-Neto, L.E.P. Borges, G. Jacobs, B.H. Davis, T. Sooknoi, D.E. Resasco, F.B. Noronha, *ACS Catal.* 5 (2015) 1318–1329.
- [12] P.M. de Souza, R.C. Rabelo-Neto, L.E.P. Borges, G. Jacobs, B.H. Davis, D.E. Resasco, F.B. Noronha, *ACS Catal.* 7 (2017) 2058–2073.
- [13] P.M. de Souza, R.C. Rabelo-Neto, L.E.P. Borges, G. Jacobs, B.H. Davis, U.M. Graham, D.E. Resasco, F.B. Noronha, *ACS Catal.* 5 (2015) 7385–7398.
- [14] A. Vicente, G. Lafaye, C. Espel, P. Marécot, C.T. Williams, *J. Catal.* 283 (2011) 133–142.
- [15] T. Ressler, *J. Synchrotron Rad.* 5 (1998) 118–122.
- [16] G. Jacobs, Y. Ji, B.H. Davis, D. Cronauer, A.J. Kropf, C.L. Marshall, *Appl. Catal. A* 333 (2007) 177–191.
- [17] B. Ravel, *J. Synchrotron Rad.* 8 (2001) 314–316.
- [18] J.J. Rehr, J.M. de Leon, S.I. Zabinsky, R.C. Albers, *J. Am. Chem. Soc.* 113 (1991) 5135–5140.
- [19] B. Ravel, M. Newville, *J. Synchrotron Rad.* 12 (2005) 537–541.
- [20] W. Khaodee, B. Jongsomjit, S. Assabumrungrat, P. Praserthdam, S. Goto, *Catal. Commun.* 8 (2007) 548–556.
- [21] B. Coq, F. Figueras, *J. Mol. Catal. A* 173 (2001) 117–134.
- [22] S. Karski, I. Wito, J. Rogowski, J. Goluchowska, *J. Mol. Catal. A* 240 (2005) 155–163.
- [23] E.B. Fox, S. Velu, M.H. Engelhard, Y. Chin, J.T. Miller, J. Kropf, C. Song, *J. Catal.* 260 (2008) 358–370.
- [24] G. Jacobs, W. Ma, P. Gao, *Top. Catal.* 55 (2012) 811–817.
- [25] M. Lesiak, M. Binczarski, S. Karski, W. Manukiewicz, J. Rogowski, E. Szubiakiewicz, J. Berlowska, P. Dziugan, I. Witońska, *J. Mol. Catal. A* 395 (2014) 337–348.
- [26] L.B. Okhlopkova, M.A. Kerzhentsev, *J. Nanopart. Res.* 14 (2012) 1088–1103.
- [27] D. Fort, J.P.G. Farr, I.R. Harris, *J. Less Common. Met.* 39 (1975) 293–308.
- [28] I.R. Harris, M. Cordey-Hayes, *J. Less Common. Met.* 6 (1968) 223–232.
- [29] A. Jentys, *Phys. Chem. Chem. Phys.* 1 (1999) 4059–4063.
- [30] D. Lahiri, B. Bunker, B. Mishra, Z. Zhang, D. Meisel, C.M. Doudna, M.F. Bertino, F.D. Blum, A.T. Tokuhiro, S. Chattopadhyay, T. Shibata, J. Terry, *J. Appl. Phys.* 97 (2005) 094304.
- [31] W. Huang, W. Pyrz, R.F. Lobo, J.G. Chen, *Appl. Catal. A* 333 (2007) 254–263.
- [32] M. Faticanti, N. Ciolfi, S. de Rossi, N. Ditaranto, P. Porta, L. Sabbatini, T. Bleve-Zacheo, *Appl. Catal. B* 60 (2005) 73–82.
- [33] M.P. Kapoor, Y. Ichihashi, W. Shen, Y. Matsumura, *Catal. Lett.* 76 (2001) 139–142.
- [34] Y. Matsumura, M. Okumura, Y. Usami, K. Kagawa, H. Yamashita, M. Anpo, M. Haruta, *Catal. Lett.* 44 (1997) 189–191.
- [35] N. Ciolfi, M. Faticanti, N. Ditaranto, S. de Rossi, L. Traversa, A. Monopoli, A. Nacci, L. Torsi, L. Sabbatini, *Curr. Nanosci.* 3 (2007) 121–127.
- [36] N. Barrabés, J. Just, A. Dafinov, F. Medina, J.L.G. Fierro, J.E. Sueiras, P. Salagre, Y. Cestero, *Appl. Catal. B* 62 (2006) 77–85.
- [37] A. Pachulski, R. Schödel, P. Claus, *Appl. Catal. A* 400 (2011) 14–24.
- [38] R.N. Lamb, B. Ngamsom, D.L. Trimm, B. Gong, P.L. Silveston, P. Praserthdam, *Appl. Catal. A* 268 (2004) 43–50.
- [39] G. Neri, C. Milone, S. Galvagno, A.P.J. Pijpers, J. Schwank, *Appl. Catal. A* 227 (2002) 105–115.
- [40] M.C. Aguirre, P. Reyes, M. Oportus, I. Melián-cabrera, J.L.G. Fierro, *Appl. Catal. A* 233 (2002) 183–196.
- [41] S. Nishiyama, T. Hara, S. Tsuruya, M. Masai, *J. Phys. Chem. B* 103 (1999) 4431–4439.
- [42] F.J. Kuijers, V. Ponec, *J. Catal.* 60 (1979) 100–109.
- [43] I. Karakaya, W.T. Thompson, *Bull. Alloy Phase Diagr.* 9 (1988) 237–243.
- [44] P.R. Subramanian, D.E. Laughlin, *J. Phase Equilibr.* 12 (1991) 2.
- [45] J. Batista, A. Pintar, D. Mandrino, M. Jenko, V. Martin, *Appl. Catal. A* 206 (2001) 113–124.
- [46] M. Fernández-García, J.A. Anderson, G.L. Haller, *J. Phys. Chem.* 100 (1996) 16247–16254.
- [47] A.M. Venezia, L.F. Liotta, G. Deganello, Z. Schay, L. Guczi, *J. Catal.* 182 (1999) 449–455.
- [48] G. Cárdenas, R. Oliva, P. Reyes, B.L. Rivas, *J. Mol. Catal.* 191 (2003) 75–86.
- [49] T. Conant, A.M. Karim, V. Lebarbier, Y. Wang, F. Girsides, R. Schlögl, A. Datye, *J. Catal.* 257 (2008) 64–70.
- [50] N. Iwasa, T. Mayanagi, S. Masuda, N. Takezawa, *React. Kinet. Catal. Lett.* 69 (2000) 355–360.
- [51] Y. Suwa, S. Ito, S. Kameoka, K. Tomishige, K. Kunimori, *Appl. Catal. A* 267 (2004) 9–16.
- [52] S. Echeandía, B. Pawelec, V.L. Barrio, P.L. Arias, J.F. Cambra, C.V. Loricera, J.L.G. Fierro, *Fuel* 117 (2014) 1061–1073.
- [53] C. Zhao, J. He, A.A. Lemonidou, X. Li, J.A. Lercher, *J. Catal.* 280 (2011) 8–16.
- [54] J. Horáček, G. Stávová, V. Kelbichová, D. Kubicka, *Catal. Today* 204 (2013) 38–45.
- [55] C. Newman, X. Zhou, B. Goundie, I.T. Ghompson, R.A. Pollock, Z. Ross, M.C. Wheeler, R. Meulenberg, R.N. Austin, B.G. Frederick, *Appl. Catal. A* 477 (2014) 64–74.
- [56] P.T.M. Do, A.J. Foster, J. Chen, R.F. Lobo, *Green Chem.* 14 (2012) 1388–1397.
- [57] H. Wan, R.V. Chaudhari, B. Subramanian, *Top. Catal.* 55 (2012) 129–139.
- [58] X. Zhu, L. Nie, L.L. Lobban, R.G. Mallinson, D.E. Resasco, *Energy Fuels* 28 (2014) 4104–4111.
- [59] E.J. Shin, M.A. Keane, *Ind. Eng. Chem. Res.* 39 (2000) 883–892.
- [60] C. Zhao, D.M. Camaiora, J.A. Lercher, *J. Catal.* 288 (2012) 92–103.
- [61] X. Zhang, T. Wang, L. Ma, Q. Zhang, X. Huang, Y. Yu, *Appl. Energy* 112 (2013) 533–538.
- [62] B. Guvenatam, O. Kurşun, E.H.J. Heeres, E.A. Pidko, E.J.M. Hensen, *Catal. Today* 233 (2013) 83–91.
- [63] C.A. Teles, R.C. Rabelo-Neto, J.R. de Lima, L.V. Mattos, D.E. Resasco, F.B. Noronha, *Catal. Lett.* 146 (2016) 1848–1857.
- [64] Q. Tan, G. Wang, L. Nie, A. Dinse, C. Buda, J. Shabaker, D.E. Resasco, *ACS Catal.* 5 (2015) 6271–6283.
- [65] P.M. de Souza, L. Nie, L.E.P. Borges, F.B. Noronha, D.E. Resasco, *Catal. Lett.* 144 (2014) 2005–2011.
- [66] N. Iwasa, M. Takizawa, M. Arai, *Appl. Catal. A* 283 (2005) 255–263.
- [67] S. Sitthisai, T. Pham, T. Prasomsri, T. Sooknoi, R.G. Mallinson, D.E. Resasco, *Catal. Lett.* 280 (2011) 17–27.